ELSEVIER

Chemical Geology 230 (2006) 60–87

CHEMICAL GEOLOGY
INCLUDING
ISOTOPE GEOSCIENCE

www.elsevier.com/locate/chemgeo

# Geochemical characteristics of the Neoarchean (2800–2700 Ma) Taishan greenstone belt, North China Craton: Evidence for plume–craton interaction

A. Polat [a,*], J. Li [b], B. Fryer [a,c], T. Kusky [d], J. Gagnon [a,c], S. Zhang [a,c]

[a] *Department of Earth Sciences, University of Windsor, Windsor, ON, Canada N9B 3P4*
[b] *Department of Geology, Peking University, Beijing 100871 China*
[c] *Great Lakes Institute for Environmental Research, University of Windsor, Windsor, ON, Canada N9B 3P4*
[d] *Department of Earth and Atmospheric Sciences, Saint Louis University, St. Louis, MO 63103, USA*

Received 12 March 2005; received in revised form 31 October 2005; accepted 20 November 2005

**Abstract**

The 2800–2700 Ma Taishan greenstone belt, North China Craton, consists of an association of komatiites, pillow basalts, banded iron formations, conglomerates, and greywacke sandstones. The belt was intruded by high-Al tonalite–trondhjemite–granodiorite (TTG) plutons and deformed under amphibolite-grade metamorphism at about 2700 Ma.

At the bottom of the association komatiites are characterized by locally well-preserved spinifex, cumulate, and breccia textures. Spinifex komatiites have uniformly high-MgO (31–33 wt.%), but low-$Al_2O_3$ (2.8–5.7 wt.%), $TiO_2$ (0.14–0.24 wt.%), and Zr (4.6–9.6 ppm) contents. Towards the top of the sequence komatiites become less magnesian (MgO=22–23 wt.%), more aluminous ($Al_2O_3$=6.2–8.9 wt.%), and display higher concentrations of incompatible elements. Based on [$Al_2O_3$] versus [$TiO_2$] molecular relations, these rocks plot mainly in the field of Al-depleted komatiites. Komatiites occurring at stratigraphically lower levels have concave-upward LREE patterns and negative Nb anomalies (Nb/Nb*=0.19–0.96). Stratigraphically upper komatiites and pillow basalts also share the negative Nb anomalies. There are strong correlations between the initial $\varepsilon_{Nd}$ values and indices of crustal contamination and olivine fractionation, suggesting that the geochemical characteristics of the Taishan komatiites can be best explained by olivine fractionation and assimilation of 2–6% LREE-enriched older continental crust or sediments.

Relict olivine grains in the Taishan komatiites have lower Mg-numbers ($Fo_{79–84}$) than whole-rock (84–90) and serpentine–chlorite–amphibole matrix (90–95), indicating that whole-rock composition is not in equilibrium with olivine composition. This disequilibrium is likely have resulted from the enrichment of Fe in recrystallized olivines during amphibolite metamorphism at ~2700 Ma.

Conglomerates are composed dominantly of gneissic, granitic, and amphibolitic clasts. Grain types and trace element characteristics of sandstones are consistent with a continental source area. There are zircon and apatite xenocrysts in the stratigraphically lower komatiites. Collectively, these geological features are consistent with the deposition of the greenstone belt on continental basement. Accordingly, we propose a geodynamic model of plume–craton interaction to explain the geological and geochemical characteristics of the Taishan greenstone belt.


*Keywords:* Archean; Greenstone belt; Komatiite; Mantle plume; North China Craton

* Corresponding author. Tel.: +1 519 253 3000 2498; fax: +1 519 973 7081.
*E-mail address:* polat@uwindsor.ca (A. Polat).

0009-2541/$ - see front matter © 2005 Elsevier B.V. All rights reserved.
doi:10.1016/j.chemgeo.2005.11.012

## 1. Introduction

Komatiites are ultramafic lavas, or shallow sills, that typically have spinifex texture and high MgO content (>18 wt.%; Arndt, 1994). Komatiites are traditionally divided into two major groups: (1) Al-depleted komatiites (ADK) and (2) Al-undepleted komatiites (AUK; Nesbitt et al., 1979; Arndt, 1994). Each group is represented by distinct $Al_2O_3/TiO_2$ and $CaO/Al_2O_3$ ratios. ADK are characterized by low $Al_2O_3/TiO_2$ ($\leq 10$) and high $CaO/Al_2O_3$ ($\sim 1.5$) ratios and depleted HREE ($Gd/Yb_{cn}=1.1–1.7$) patterns. In contrast, AUK possess near-chondritic $Al_2O_3/TiO_2$ ($\sim 20$) and $CaO/Al_2O_3$ ($\sim 1$) ratios with flat HREE ($Gd/Yb_{cn}=0.9–1.1$) patterns.

Al-undepleted komatiites are the most common types of komatiite in Neoarchean greenstone belts (Dostal and Mueller, 2004). Herzberg (1992) and Nisbet et al. (1993) proposed that ADK, which predominantly occur in Mesoarchean greenstone belts, were generated at higher mantle potential temperatures than AUK, which is supported by geochemical signatures of β-majorite garnet signifying melting below 400 km (Xie et al., 1993). Highly magnesian olivines present in both ADK and AUK require that they were in equilibrium with liquids containing commensurately high-MgO (~29 wt. %) contents (Nisbet et al., 1993; Renner et al., 1994; Herzberg, 2004).

The geochemical characteristics of Archean komatiites are of particular interest in understanding early mantle evolution, petrogenesis, and geodynamic processes (Nesbitt et al., 1979; Nisbet, 1982; Sun, 1987; Jochum et al., 1991; Arndt, 1994; Gibson, 2002; Wilson, 2003; Wilson et al., 2003; Grove and Parman, 2004). It is generally accepted that komatiites are anhydrous liquids erupting at high-temperatures (~1600 °C), and their origin has been attributed to anomalously hot plumes rising from deep mantle, erupting either as intra-oceanic plateaus or through continental crust (Herzberg, 1992, 2004; McDonough and Ireland, 1993; Xie et al., 1993; Kerr et al., 1996; Arndt et al., 1998; Puchtel et al., 1998, 1999; Sproule et al., 2002). Alternatively, Parman et al. (1997, 2001, 2003) proposed a subduction zone origin for the Barberton komatiites.

On the basis of the presence of spinifex textures, ultramafic rocks in the Neoarchean Taishan greenstone belt were classified as komatiites in the early 1990s (Xu et al., 1992; Cao et al., 1996; Ma, 1996; Zhang et al., 2001; and references therein). To our knowledge, no comprehensive geochemical data have been reported for the Taishan komatiites. Accordingly, we sampled komatiites with locally well-preserved spinifex textures and fresh olivines, and spatially associated pillow basalts, and overlying greywacke sandstones (Figs. 1–4). We report high-precision trace element and Nd isotope data for komatiites, and trace element data for

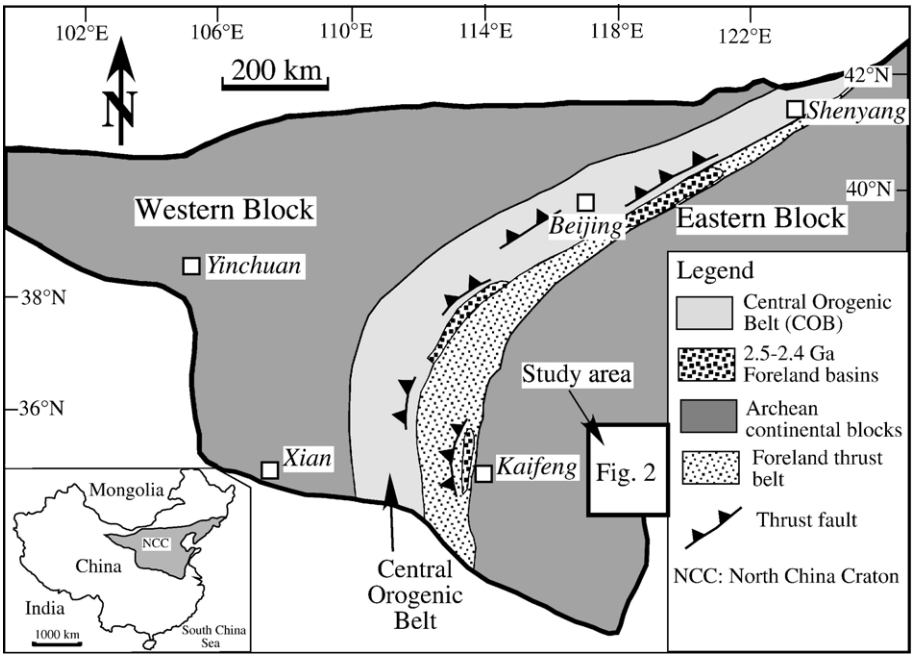


Fig. 1. Simplified geological map of the North China Craton showing the major tectonic divisions and location of the study area (modified after Kusky and Li, 2003).

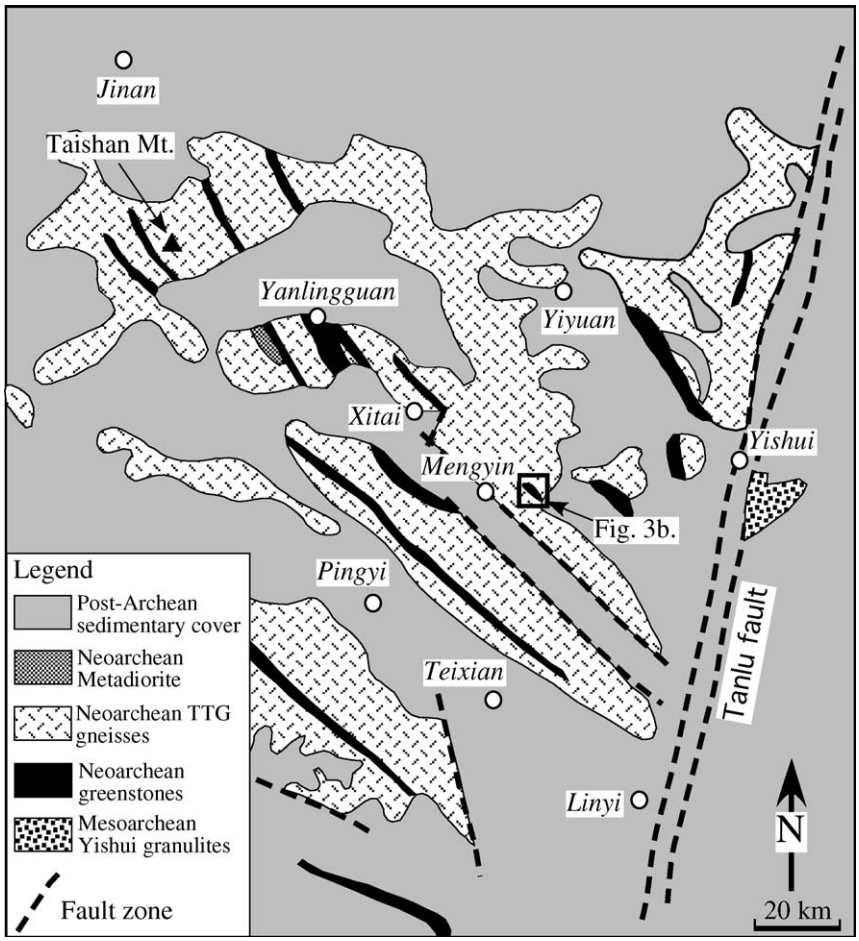


Fig. 2. Simplified geological map of the study area (modified after Zhang et al., 2001).

basalts and greywacke sandstones. In addition, we report electron microprobe major element data for olivines and serpentine–chlorite–amphibolite matrix in spinifex and cumulate komatiites. The objectives of this paper are two-fold: (1) to characterize the petrogenesis of komatiites and associated basalts, and (2) to understand the geodynamic evolution of the Taishan greenstone belt.

## 2. Regional geology and geochronology

The West Shandong Metamorphic Terrane, constitutes a major part of the Shandong Mountains, Shandong Province, in the central-east sector of the North China Craton (Figs. 1 and 2). This terrane records a prolonged history of multiple metamorphic, magmatic, and deformation events extending from 3000 to 2400 Ma (Cao et al., 1996; Xu et al., 1992; Ma, 1996; Wu et al., 1991, 1998). The oldest rocks in the region are the 3000–2900 Ma mafic to ultramafic granulites termed the Yishui Group located to the east of the study area (Cao et al., 1996). Yishui granulites are separated from the Taishan greenstone belt by the Tanlu fault zone (Fig. 2).

The study area is dominated (~95%) by variably metamorphosed Neoarchean (2800–2500 Ma) intrusive rocks, including diorites, monzonites, monzogranites, monzodiorites, gabbros, synites, tonalite–trondhjemite–granodiorite (TTG) suite, and granites (Fig. 2; Cao et al., 1996; Wu et al., 1991, 1998). The 2800–2700 Ma old volumetrically minor ultramafic to felsic volcanic and sedimentary rocks, collectively known as the Taishan greenstone belt, or Taishan Group, occur as lenses within the TTG gneisses (Fig. 2; Xu et al., 1992; Cao et al., 1996; Zhang et al., 2001).

Jahn et al. (1988) and Cao et al. (1996) provided a detailed description of the isotopic, trace element, and geochronological characteristics of the West Shandong Metamorphic Terrane. The TTG gneisses yielded a whole rock Rb–Sr isochron age of 2767±45 Ma. A low initial $^{87}Sr/^{86}Sr$ value (0.7006±4) suggests that the

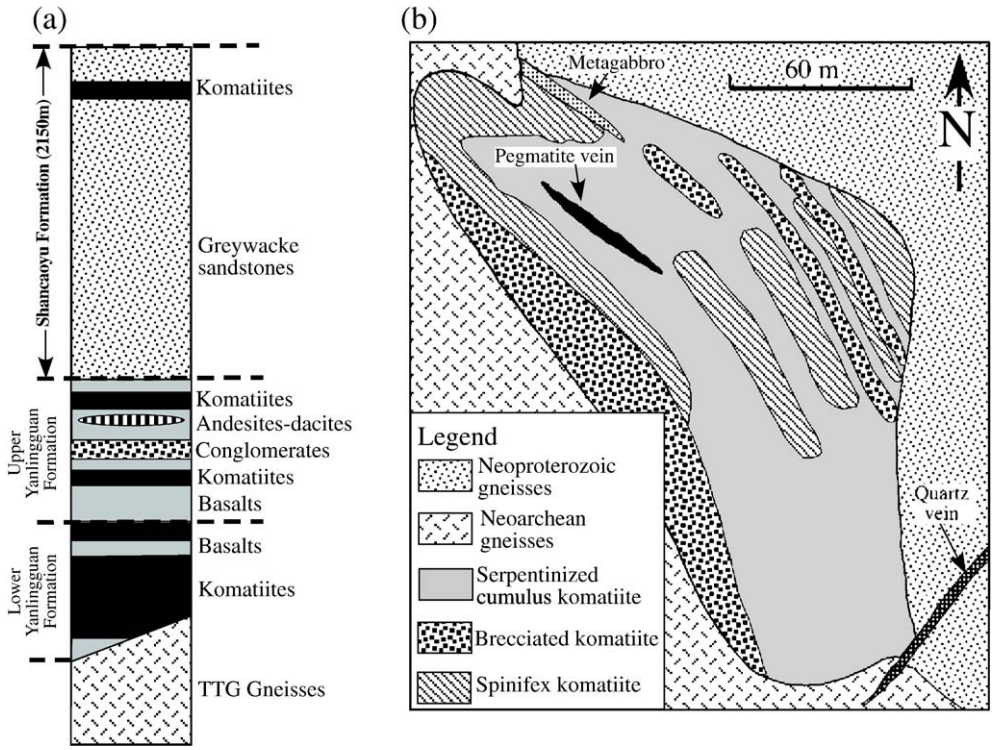


Fig. 3. (a) Simplified volcano-sedimentary stratigraphy of the Taishan greenstone belt (modified after Xu et al., 1992). (b) Detailed geological map of komatiite exposures in the lower Yanlingguan Formation near the village of Sujiagou in Menying County (modified after Zhang et al., 2001).

protoliths for the TTG gneisses originated from a depleted mantle source. Regression of whole-rock Sm–Nd data for the TTG gneisses and amphibolite inclusions yielded an isochron age of 2700±35 Ma. Epsilon-Nd (2700 Ma) of +3.3±0.3 is also consistent with a long-term depleted mantle for the protoliths. The amphibolite inclusions alone yielded an age of 2740±70 Ma. Because the Sm–Nd isotopic system is more resistant to post-magmatic alteration and metamorphic processes, Jahn et al. (1988) interpreted the isochron age of 2740±70 Ma for the amphibolites to represent the time of emplacement of the basaltic magmas.

Felsic volcanic rocks in the upper Yanlingguan Formation yielded a U–Pb zircon age of 2788+62/−56 Ma (Wu et al., 1998). However, no cathodoluminescence image analyses were conducted; accordingly it could either represent an inherited zircon or the age of felsic volcanism. Diorites intruding the Yanlingguan Formation have a U–Pb zircon age of 2699+30/−28 Ma (Xu et al., 1992; Wu et al., 1998), constraining the minimum age of the Taishan greenstone belt.

The greenstone belt was metamorphosed at amphibolite grade (~550 °C), intruded by TTG suites, and deformed at ~2700 Ma. The belt underwent an upper greenschist to lower amphibolite facies (~450 °C) metamorphism and intrusion by a gabbroic to dioritic suite between 2600 and 2400 Ma (Cao et al., 1996).

## 3. Field characteristics and petrography

In the lower Yanlingguan Formation, the contact between komatiites and the underlying TTG gneisses is intrusive to sheared (Fig. 3). Komatiites have a tectonostratigraphic thickness of about 400 m; they are characterized by variably deformed layers of cumulates, platy and randomly oriented spinifex, and flow top breccia (Figs. 4 and 5; Xu et al., 1992; Wu et al., 1991; Cao et al., 1996; Zhang et al., 2001; this study). At stratigraphically higher levels in the formation komatiite flows are thinner, primary textures are obliterated due to penetrative deformation, and the intensity of carbonate–silica alteration increases. Higher in the formation komatiites are structurally intercalated with tholeiitic pillow basalts, minor calc-alkaline andesites to dacites, conglomerates, sandstones, and banded iron formations. Conglomerates include gneissic, granitic, and amphibolitic pebbles (Figs. 3 and 5; Xu et al., 1992; Cao et al., 1996; Wu et al., 1998; Zhang et al., 2001).

Lower in the formation komatiites have relatively simple mineral assemblages and locally well-preserved

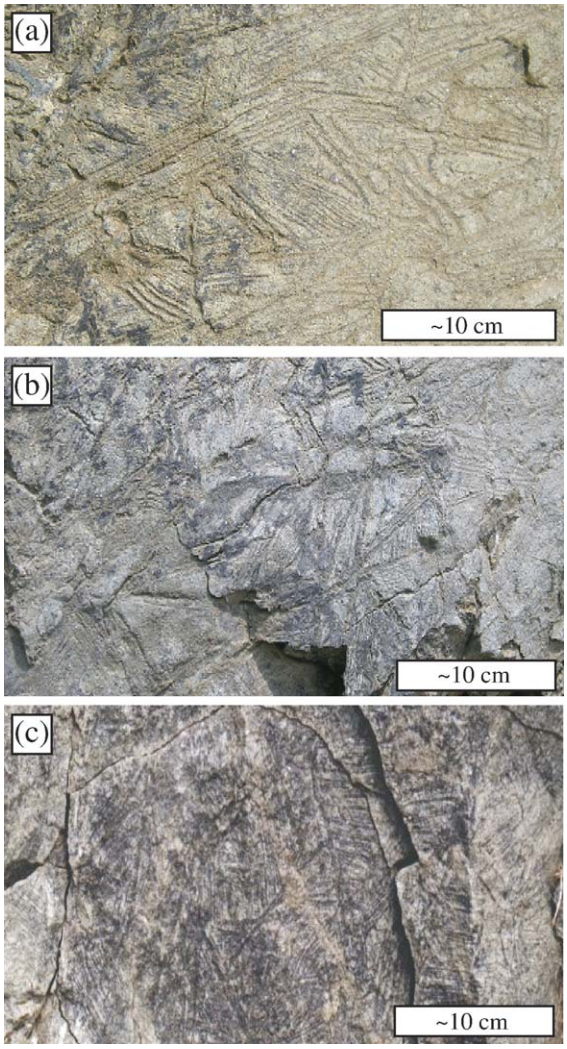


Fig. 4. Spinifex textures in the lower Yanlingguan Formation (samples 2004-12A, 2004-15B).

igneous textures (Fig. 4). Olivine is modally ~30% in spinifex and cumulate domains, with magnetite (Fig. 5). The platy spinifex is characterized by blades 1–3-mm thick and up to 100-mm long (Fig. 4). Interstitial space between spinifex and cumulate olivine is filled by devitrified glass and opaque minerals. Where the original spinifex texture has been preserved primary olivines have been replaced by metamorphic olivine + serpentine + chlorite + actinolite + tremolite ± magnetite under amphibolite facies conditions. Glass is devitrified to an assemblage of chlorite + actinolite + serpentine ± tremolite ± talc. Relict olivine grains in the cumulus layers are enclosed in a matrix of fine-grained serpentine + chlorite ± talc. Xenocrystic zircons and apatites have been reported in these komatiites (Zhang et al., 2001).

Higher in the formation komatiites are composed dominantly of actinolite + tremolite + chlorite ± carbonate (calcite, dolomite) ± quartz ± magnetite. No spinifex or cumulate textures are preserved. Pillow basalts are composed mainly of hornblende + plagioclase + epidote + quartz ± titanite ± carbonate ± sulphide. Greywacke sandstones are composed primarily of rock fragments + quartz + plagioclase + muscovite.

## 4. Sampling and analytical procedures

Komatiite samples were collected from both the lower and upper sections, whereas pillow basalts were collected only from the upper section of the Yanlingguan Formation (Fig. 3a). Sandstones were collected from the Shancaoyu Formation.

All samples were powdered using an agate mill. Major elements were determined by a Rigaku RIX 3000 XRF spectrometer at the Ontario Geological Survey, Sudbury, Canada. Totals of major element oxides are 100 ± 1 wt.% and the analytical precisions are 2 to 4%.

Samples were analysed for rare earth elements (REE), high field strength elements (HFSE), large ion lithophile elements (LILE), and transition metals (Ni, Co, Cr, V, Sc) by a high-sensitivity ThermoElemental X7 ICP-MS at the Great Lakes Institute for Environmental Research (GLIER), University of Windsor, Ontario, Canada, using the protocols of Jenner et al. (1990). Wet chemical procedures were conducted under clean lab conditions, and all acids were distilled twice. All samples were analyzed twice, using the $HF–HNO_3$ and $Na_2O_2$ sinter techniques to circumvent potential problems associated with HFSE (e.g., Zr, Hf, Nb, Ta) and REE in refractory minerals. Approximately 100–150 mg of sample powder was used for dissolution and sintering. Samples were dissolved in a concentrated $HF–HNO_3$ mixture at a temperature of ~120 °C for four days, and then further attacked with concentrated $HNO_3$ until no residue was visible. BIR-1 and BHVO-2 were used as international reference materials to estimate precision and accuracy (Table 1). Analytical precisions are estimated as follows: 1% to 10% for REE, Rb, Li, Cs, Sr, Ba, Y, Cu, Zn, and Pb; 10% to 20% for Zr, V, Cr, Ni, Co, and U; and 20% to 30% for Nb, Ta and Th.

Analyses of olivines in polished thin sections were performed on a JEOL 8600 Superprobe electron microprobe analyzer (EMPA) in the Department of Geological Sciences at the University of Saskatchewan, Saskatoon, Canada. The operating conditions of the EMPA during analysis were as follows: accelerator

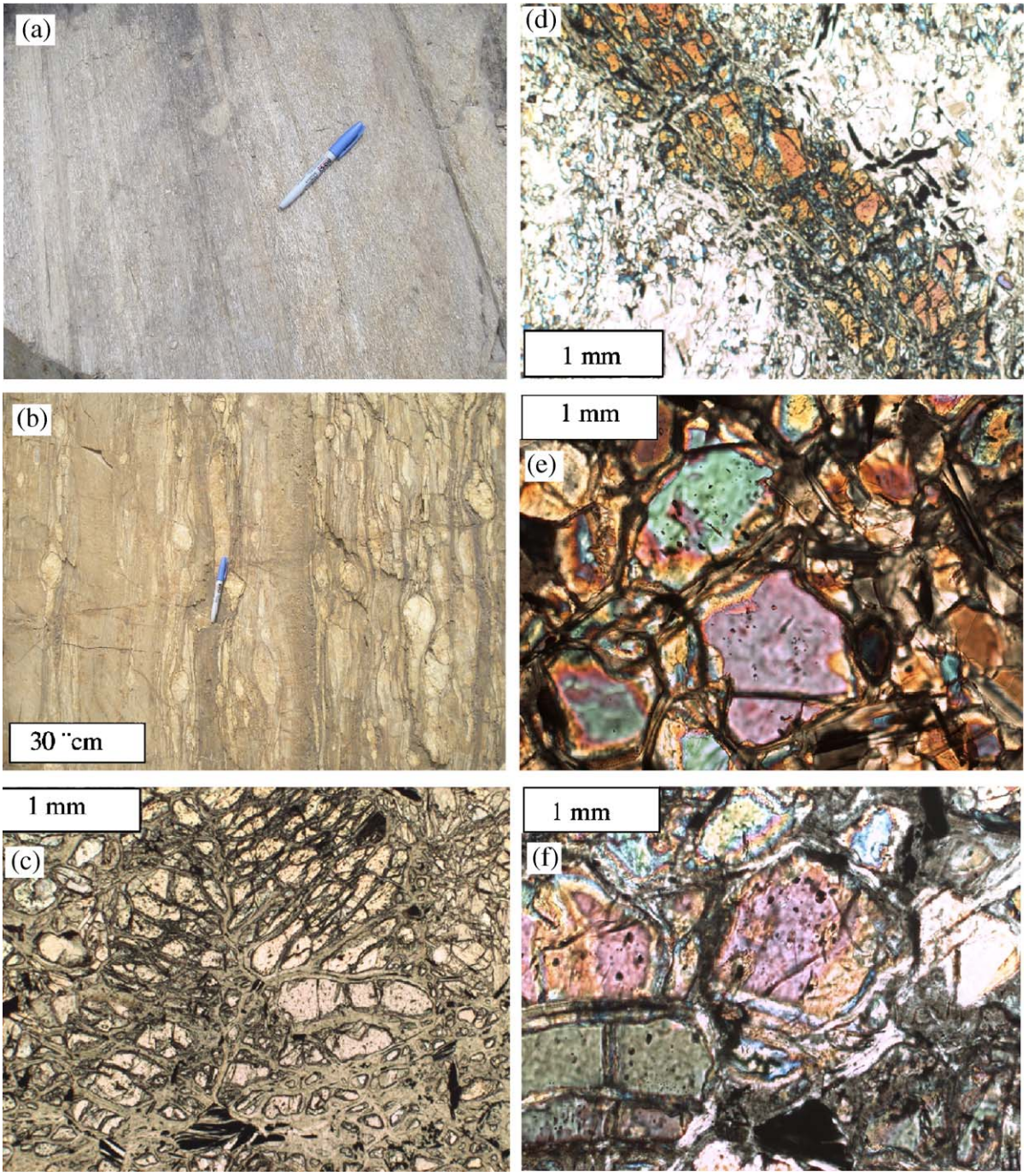


Fig. 5. (a–b) Photographs of greywacke sandstones and conglomerates. (c–d) Photomicrographs of olivines in spinifex (samples KM25, 2004-12A) and (e–f) cumulate (samples 2004-09A, 2004-14A) layers. The presence of mineral inclusions (magnetite) is consistent with recrystallization of olivines during metamorphism.

voltage = 15 kV; beam current = 50 nA; and beam size = 5 μm. X-ray counts were measured at the peak centres for 30 s and at two background positions for 15 s for each element except Ca, Cr and Ni, during both calibration and analyses. The peak centre count times for Ca, Cr, and Ni were 60 s while count times for each background position were 30 s. Background measurements were taken 4 nm above and 5 nm below each peak

Table 1
Measured concentrations of USGS standards BIR-1 and BHVO-2

| Element | BIR-1 ($N$=8) | Recommended | Deviation (%) | BHVO-2 ($n$=10) | Recommended | Deviation (%) |
|---|---|---|---|---|---|---|
| Li | 2.64 | 3.10 | 17 | 4.32 | 5.0 | 16 |
| V | 348 | 310 | 11 | 328 | 317 | 3 |
| Cr | 398 | 370 | 7 | 284 | 280 | 1 |
| Co | 52 | 52 | 0 | 42 | 45 | 7 |
| Ni | 172 | 170 | 1 | 115 | 119 | 3 |
| Cu | 121 | 125 | 3 | 130 | 127 | 2 |
| Zn | 63 | 70 | 11 | 107 | 103 | 4 |
| Rb | 0.19 | 0.23 | 21 | 8.69 | 9.80 | 13 |
| Sr | 107 | 111 | 4 | 368 | 389 | 6 |
| Y | 13.4 | 15.6 | 17 | 23 | 26 | 15 |
| Zr | 13.7 | 16.3 | 19 | 158 | 172 | 9 |
| Nb | 0.48 | 0.59 | 23 | 15 | 18 | 20 |
| Cs | 0.01 | 0.01 | 10 | 0.09 | | |
| Ba | 6.60 | 6.40 | 3 | 125 | 130 | 4 |
| La | 0.60 | 0.60 | 0 | 14.23 | 15 | 5 |
| Ce | 1.88 | 1.87 | 1 | 35.73 | 38 | 6 |
| Pr | 0.37 | 0.36 | 3 | 4.96 | | |
| Nd | 2.36 | 2.30 | 3 | 22.8 | 25.0 | 10 |
| Sm | 1.09 | 1.06 | 3 | 5.69 | 6.20 | 9 |
| Eu | 0.51 | 0.56 | 10 | 1.96 | | |
| Gd | 1.83 | 1.73 | 5 | 6.13 | 6.30 | 3 |
| Tb | 0.35 | 0.36 | 3 | 0.89 | 0.90 | 1 |
| Dy | 2.46 | 2.69 | 9 | 5.07 | | |
| Ho | 0.57 | 0.61 | 7 | 0.93 | 1.04 | 12 |
| Er | 1.67 | 1.70 | 2 | 2.39 | | |
| Tm | 0.24 | 0.24 | 0 | 0.31 | | |
| Yb | 1.61 | 1.63 | 1 | 1.84 | 2.00 | 9 |
| Lu | 0.24 | 0.25 | 4 | 0.25 | 0.28 | 2 |
| Ta | 0.06 | 0.09 | 50 | 0.92 | 1.40 | 52 |
| Pb | 3.03 | 3.30 | 9 | 1.58 | | |
| Th | 0.05 | 0.04 | 20 | 1.53 | 1.20 | 21 |
| U | 0.01 | 0.01 | 0 | 0.40 | | |

for Si, Al, Mg, and Na. Background measurements for the remaining elements were taken 4 nm above and below peak centres. An in-house forsterite standard, acquired from the Smithsonian Institute, was analyzed at the beginning and the end of each of two analytical sessions (Table 2).

Table 2
Measured values for Smithsonian forsterite standard

| Element % | Smithsonian fosterite ($n$=5) | Recommended |
|---|---|---|
| Si | 19.04 | 19.10 |
| Ti | 0.00 | N.R. |
| P | 0.00 | 0.00 |
| Al | 0.01 | N.R. |
| Cr | 0.01 | N.R. |
| Fe | 7.61 | 7.42 |
| Mg | 29.58 | 29.80 |
| Mn | 0.12 | 0.11 |
| Ni | 0.30 | 0.29 |
| Ca | 0.06 | 0.03 |
| Na | 0.01 | N.R. |
| O | 43.50 | 43.25 |
| Total | 100.25 | 100.23 |

*N.R.: Not Recommended.

The Sm–Nd isotope analyses of a subset of samples were carried out at Carleton University, Ottawa, Canada. Whole-rock powders were leached in 2$N$ HCl at ~120 °C for 24 h, and then washed with milli-Q™ ultrapure $H_2O$. Between 2 and 2.5 g of sample powder were weighed into a 60-ml screw-cap Savillex vial, into which a mixed $^{148}Nd$–$^{149}Sm$ spike was added. The powder–spike mixture was dissolved in HF at ~120 °C for a month, resulting in ~90% dissolution. This was followed by dissolution in 7$N$ $HNO_3$ at ~120 °C for one week, further attacked by 6$N$ HCl at ~120 °C for three weeks until no residue was visible, and finally attacked by 2.5$N$ HCl for two weeks. Because of large sample weight, the HCl solution was split into six Sr columns so as not to oversaturate the columns in cations. The REE-bearing acid from the six columns were then mixed and dried together so that the REE for

one sample could go through one column. The bulk REE were separated using cation chromatography (Dowex 50-X8). The REE-bearing residue was dissolved in 0.26*N* HCl and loaded into a 10-ml borosilicate glass chromatographic column containing a 2-cm high bed of Teflon™ powder coated with HDEHP [di(2-ethylhexyl) orthophosphoric acid (Richard et al., 1976). Neodymium was eluted using 0.26*N* HCl, followed by Sm in 0.5*N* HCl. Samples were loaded with 0.3*N* $H_3PO_4$ on one side of a Re double filament assembly, and run at temperatures of 1800–1850 °C in a Finnigan MAT261 multicollector mass spectrometer. Isotope ratios were normalized to $^{146}Nd/^{144}Nd=0.72190$. Analyses of the USGS standard BCR-1 yielded Nd=29.02 ppm, Sm=6.68 ppm, and $^{143}Nd/^{144}Nd=0.512668\pm20$ ($n=4$). Over 70 runs of the La Jolla standard averaged $^{143}Nd/^{144}Nd=0.511876\pm 18$. Total procedural blanks of four analyses for Nd were between 42 and 121 pg. The concentrations of Sm and Nd are precise to ±1%, but $^{147}Sm/^{144}Nd$ ratios are reproducible to 0.5%. There is a good agreement between high-sensitivity ICP-MS and TIMS analyses for Sm and Nd concentrations (Tables 3 and 6). The initial $\varepsilon_{Nd}$ values were calculated based on the present-day $^{147}Sm/^{144}Nd$ and $^{143}Nd/^{144}Nd$ of the Chondrite Uniform Reservoir (CHUR) of 0.1967 and 0.512638, respectively, (Jacobsen and Wasserburg, 1980). Uncertainties in calculated epsilon values are ±0.5 epsilon units, based on results of duplicate runs.

## 5. Geochemical results

### 5.1. Whole-rock major and trace elements

#### 5.1.1. Komatiites

Komatiites lower in the formation have unusually high MgO (35–41 wt.% in cumulates and 31–33 wt.% in spinifex layers) compared to other ADK. Similarly, Ni (1870–2740 ppm in cumulates and 1330–2000 ppm in spinifex layers), and Cr (1600–5040 ppm in cumulates and 1690–5760 ppm in spinifex layers) contents are high, but $TiO_2$ (0.10–0.14 in cumulates and 0.10–0.24 wt.% in spinifex layers) is low relative to other komatiites (Fig. 6; Table 3; Arndt, 1994; Dostal and Mueller, 2004). They have narrow ranges of Mg-numbers (86–90 in cumulates and 84–87 in spinifex layers) and $SiO_2$ (45–48 wt.%) contents. In addition, they are depleted in LILE, REE, and HFSE (Fig. 7; Table 3).

Lower komatiites are characterized by variably sub-chondritic Nb/Ta (11–17), but super-chondritic Ti/Zr (140–310) and $Al_2O_3/TiO_2$ (23–32) ratios. Cumulate layers display LREE-depleted to enriched ($La/Sm_{cn}=0.61–1.97$) patterns, whereas the spinifex layers possess LREE-depleted ($La/Sm_{cn}=0.61–0.75$) patterns (Fig. 8). Both cumulate and spinifex groups have moderately depleted to flat HREE patterns ($Gd/Yb_{cn}=0.81–1.08$ in cumulates and $Gd/Yb_{cn}=0.83–1.10$ in spinifex layers). On a primitive mantle-normalized diagram, they display variably negative Nb and Zr troughs (Fig. 8; Table 3).

Komatiites higher in the formation have relatively lower MgO (22.5–29.6 wt.%) and Ni (320–1770 ppm), but higher $SiO_2$ (46.5–51.1 wt.%), $Al_2O_3$ (6.2–8.9 wt.%), and CaO (5.3–9.4 wt.%) contents than stratigraphically lower counterparts (Tables 3 and 4). Chondrite- and primitive mantle-normalized patterns are comparable to komatiites lower in the section, excepting more pronounced fractionation of LREE-MREE in some samples (Fig. 8). $Al_2O_3/TiO_2$ ratios (11–29) range from sub- to super-chondritic (Table 4).

#### 5.1.2. Pillow basalts

Pillow basalts are characterized by 48–52 wt.% $SiO_2$, 5–17 wt.% MgO, 7–16 wt.% $Al_2O_3$, 0.36–0.93 wt.% $TiO_2$, and 100–580 ppm Ni (Fig. 6; Table 4). $Al_2O_3/TiO_2$ ratios (13–22) and primitive mantle-normalized patterns are similar to those of associated komatiites (Fig. 8d, h; $La/Sm_{cn}=0.80–1.76$; $Gd/Yb_{cn}=1.10–1.60$; $Nb/Nb^*=0.30–0.80$).

#### 5.1.3. Sandstones

Sandstones are typically enriched in $SiO_2$ (63–72 wt.%), $Al_2O_3$ (14.8–18.2 wt.%), $Na_2O$ (3.4–5.5 wt.%), and $K_2O$ (2.4–2.8 wt.%), but have low MgO (1.0–1.6 wt.%), $Fe_2O_3$ (3.4–4.5 wt.%), $TiO_2$ (0.35–0.42 wt.%), Cr (50–96 ppm), and Ni (14–36 ppm) concentrations relative to the average Archean and present-day upper continental crusts (Table 4; see Taylor and McLennan, 1995; Rudnick and Gao, 2004). They have higher $Al_2O_3/TiO_2$ (41–44) and Zr/Y (7.8–19), but lower Ti/Zr (17–32) ratios than the Archean upper continental crust (Taylor and McLennan, 1995). On a primitive mantle-normalized diagram, they have the following characteristics: (1) positively fractionated patterns ($La/Sm_{cn}=4.5–6.0$; $Gd/Yb_{cn}=1.8–2.4$); and (2) negative Nb ($Nb/Nb^*=0.13–0.14$) and Ti ($Ti/Ti^*=0.29–0.44$) anomalies (Fig. 9a).

### 5.2. Electron microprobe olivine analyses

Cumulate olivines have higher MgO (43.9–44.4 versus 40.5–42.1 wt.%) but lower FeO (14.7–15.0

Table 3
Major and trace element concentrations and selected element ratios for komatiites in the lower Yanlingguan Formation, Taishan greenstone belt

| | Cumulus texture | | | | | | | |
|---|---|---|---|---|---|---|---|---|
| | 2004-13 | 2004-10 | 2004-09B | 2004-09A | KM37 | 2004-12B | KM33 | 2004-14A |
| $SiO_2$ | 44.79 | 45.15 | 45.42 | 45.63 | 45.58 | 45.13 | 45.62 | 45.88 |
| $TiO_2$ | 0.11 | 0.10 | 0.11 | 0.12 | 0.12 | 0.12 | 0.11 | 0.14 |
| $Al_2O_3$ | 2.83 | 2.75 | 3.53 | 3.90 | 3.36 | 3.59 | 3.23 | 4.28 |
| $Fe_2O_3$ | 9.07 | 9.05 | 9.89 | 10.07 | 9.90 | 11.24 | 10.14 | 10.04 |
| MnO | 0.16 | 0.15 | 0.15 | 0.15 | 0.14 | 0.16 | 0.15 | 0.15 |
| MgO | 40.84 | 40.57 | 37.73 | 36.79 | 36.02 | 35.94 | 35.85 | 35.21 |
| CaO | 2.10 | 2.16 | 3.07 | 3.02 | 4.63 | 3.63 | 4.66 | 4.06 |
| $K_2O$ | 0.09 | 0.04 | 0.06 | 0.12 | n.d. | 0.05 | n.d. | 0.07 |
| $Na_2O$ | 0.01 | 0.01 | 0.02 | 0.19 | 0.24 | 0.12 | 0.24 | 0.15 |
| LOI | 11.24 | 10.86 | 10.37 | 9.70 | 10.57 | 8.52 | 10.52 | 8.75 |
| Mg-number | 89.9 | 89.9 | 88.3 | 87.9 | 87.8 | 86.4 | 87.5 | 87.4 |
| P | n.d. | n.d. | n.d. | n.d. | 27.64 | n.d. | 24.31 | n.d. |
| Cr | 2397 | 4484 | 4600 | 4738 | 2361 | 5038 | 1605 | 5022 |
| Co | 69 | 109 | 108 | 107 | 104 | 117 | 99 | 106 |
| Ni | 2581 | 2737 | 2427 | 2325 | 2040 | 2366 | 1871 | 2131 |
| Rb | 1.13 | 0.71 | 0.72 | 3.03 | 0.26 | 0.82 | 0.24 | 1.68 |
| Sr | 7.7 | 8.8 | 10.4 | 22.0 | 15.0 | 12.6 | 14.4 | 21.6 |
| Cs | 0.35 | 0.27 | 0.26 | 0.39 | 0.11 | 0.38 | 0.11 | 0.51 |
| Ba | 10 | 3 | 3 | 13 | 7 | 31 | 10 | 19 |
| Sc | n.d. | n.d. | n.d. | n.d. | n.d. | n.d. | n.d. | n.d. |
| V | 30 | 77 | 88 | 91 | 81 | 100 | 65 | 108 |
| Ta | 0.01 | 0.01 | 0.01 | 0.02 | 0.01 | 0.01 | 0.01 | 0.02 |
| Nb | 0.16 | 0.12 | 0.18 | 0.37 | 0.11 | 0.16 | 0.10 | 0.25 |
| Zr | 2.17 | 2.44 | 2.79 | 2.89 | 4.11 | 5.43 | 4.42 | 4.89 |
| Th | 0.20 | 0.04 | 0.11 | 0.28 | 0.02 | 0.04 | 0.02 | 0.15 |
| U | 0.05 | 0.06 | 0.02 | 0.07 | 0.01 | 0.17 | 0.02 | 0.03 |
| Y | 2.60 | 2.41 | 2.62 | 2.94 | 3.16 | 4.73 | 2.73 | 3.46 |
| Cu | 8.1 | 4.5 | 15.6 | 10.5 | 8.9 | 15.1 | 7.6 | 4.1 |
| Zn | 57 | 72 | 76 | 87 | 67 | 87 | 55 | 73 |
| Mo | 0.25 | 0.19 | 0.92 | 0.50 | 0.28 | 0.11 | 0.25 | 0.95 |
| Pb | 4.56 | 2.98 | 3.62 | 3.36 | 4.41 | 2.77 | 3.71 | 1.43 |
| Bi | 0.15 | 0.12 | 0.41 | 0.23 | 0.36 | 0.38 | 0.86 | 0.18 |
| Li | 1.96 | 3.26 | 8.43 | 5.28 | 4.78 | 6.14 | 4.41 | 4.74 |
| La | 0.45 | 0.22 | 0.30 | 0.92 | 0.21 | 0.27 | 0.20 | 0.66 |

| | | | | | | | | |
|---|---|---|---|---|---|---|---|---|
| Ce | 1.05 | 0.53 | 0.72 | 1.98 | 0.55 | 0.66 | 0.51 | 1.53 |
| Pr | 0.13 | 0.08 | 0.10 | 0.25 | 0.09 | 0.10 | 0.09 | 0.20 |
| Nd | 0.62 | 0.43 | 0.51 | 1.05 | 0.49 | 0.54 | 0.47 | 0.93 |
| Sm | 0.19 | 0.17 | 0.19 | 0.30 | 0.22 | 0.22 | 0.19 | 0.30 |
| Eu | 0.08 | 0.07 | 0.09 | 0.12 | 0.10 | 0.10 | 0.09 | 0.11 |
| Gd | 0.32 | 0.30 | 0.32 | 0.42 | 0.36 | 0.45 | 0.33 | 0.48 |
| Tb | 0.06 | 0.06 | 0.06 | 0.07 | 0.07 | 0.10 | 0.07 | 0.08 |
| Dy | 0.43 | 0.42 | 0.46 | 0.54 | 0.51 | 0.71 | 0.46 | 0.62 |
| Ho | 0.09 | 0.09 | 0.10 | 0.12 | 0.12 | 0.17 | 0.11 | 0.13 |
| Er | 0.27 | 0.28 | 0.28 | 0.32 | 0.38 | 0.51 | 0.35 | 0.38 |
| Tm | 0.04 | 0.04 | 0.04 | 0.05 | 0.06 | 0.07 | 0.05 | 0.06 |
| Yb | 0.26 | 0.27 | 0.30 | 0.33 | 0.36 | 0.45 | 0.34 | 0.37 |
| Lu | 0.04 | 0.04 | 0.05 | 0.05 | 0.05 | 0.06 | 0.05 | 0.06 |
| $La/Yb_{cn}$ | 1.23 | 0.60 | 0.72 | 2.01 | 0.41 | 0.44 | 0.43 | 1.27 |
| $La/Sm_{cn}$ | 1.56 | 0.84 | 1.02 | 1.97 | 0.61 | 0.79 | 0.70 | 1.43 |
| $Gd/Yb_{cn}$ | 1.00 | 0.91 | 0.88 | 1.08 | 0.81 | 0.83 | 0.81 | 1.06 |
| Eu/Eu* | 0.95 | 0.94 | 1.10 | 1.01 | 1.04 | 0.98 | 1.08 | 0.86 |
| Ce/Ce* | 1.07 | 0.99 | 1.02 | 1.02 | 0.97 | 0.97 | 0.95 | 1.04 |
| $Al_2O_3/TiO_2$ | 25 | 28 | 32 | 32 | 28 | 30 | 29 | 30 |
| $CaO/Al_2O_3$ | 0.74 | 0.78 | 0.87 | 0.78 | 1.38 | 1.01 | 1.45 | 0.95 |
| Zr/Y | 0.83 | 1.01 | 1.06 | 0.98 | 1.30 | 1.15 | 1.62 | 1.41 |
| Ti/Zr | 309 | 245 | 237 | 249 | 177 | 132 | 150 | 173 |
| Ti/V | 22.03 | 7.76 | 7.52 | 7.95 | 8.95 | 7.19 | 10.12 | 7.87 |
| Ti/Ti* | 1.12 | 1.08 | 1.11 | 0.83 | 1.06 | 0.94 | 1.09 | 0.92 |
| Nb/Ta | 11.7 | 16.1 | 16.7 | 16.5 | 14.2 | 14.9 | 11.2 | 15.2 |
| Y/Ho | 28.1 | 26.5 | 26.5 | 25.4 | 26.1 | 27.7 | 24.3 | 25.9 |
| $Nb/La_{pm}$ | 0.35 | 0.55 | 0.61 | 0.40 | 0.55 | 0.58 | 0.49 | 0.38 |
| $Nb/Th_{pm}$ | 0.11 | 0.38 | 0.22 | 0.17 | 0.77 | 0.54 | 0.82 | 0.22 |
| Nb/Nb* | 0.19 | 0.46 | 0.37 | 0.26 | 0.65 | 0.56 | 0.64 | 0.29 |
| $Zr/Sm_{pm}$ | 0.46 | 0.56 | 0.59 | 0.38 | 0.74 | 0.98 | 0.94 | 0.66 |
| East | 118°.11.28′ | 118°.11.29′ | 118°.11.26′ | 118°.11.26′ | | 118°.11.23′ | | 118°.11.20′ |
| North | 35°.46.52′ | 35°.46.60′ | 35°.46.65′ | 35°.46.65′ | | 35°.46.53′ | | 35°.46.52′ |

*(continued on next page)*

Table 3 (*continued*)

| | Spinifex texture | | | | | | | | | | | | | | | | | |
|---|---|---|---|---|---|---|---|---|---|---|---|---|---|---|---|---|---|---|
| | KM7B | KM25 | KM40 | KM2A | 2004-15B | KM3A | KM7A | KM5 | KM16A | 04-15A | KM38 | KM3B | 2004-12A | 2004-14B | KM4 | 2004-11A | KM2B | KM16B |
| $Al_2O_3$ | 4.03 | 4.07 | 5.08 | 5.55 | 4.79 | 5.17 | 4.94 | 4.90 | 5.12 | 4.66 | 4.97 | 5.40 | 3.40 | 4.97 | 5.70 | 4.97 | | |
| $Fe_2O_3$ | 12.11 | 12.38 | 10.66 | 9.93 | 11.00 | 10.11 | 10.33 | 10.12 | 10.19 | 10.46 | 9.79 | 9.64 | 10.84 | 9.33 | 9.17 | 9.93 | | |
| MnO | 0.16 | 0.14 | 0.16 | 0.14 | 0.17 | 0.14 | 0.15 | 0.16 | 0.15 | 0.17 | 0.15 | 0.14 | 0.19 | 0.16 | 0.13 | 0.16 | | |
| MgO | 33.41 | 33.33 | 32.67 | 32.45 | 32.35 | 31.79 | 31.67 | 31.61 | 31.49 | 31.45 | 31.34 | 31.20 | 31.15 | 30.97 | 30.70 | 30.59 | | |
| CaO | 5.05 | 4.79 | 5.58 | 5.83 | 5.27 | 6.19 | 6.25 | 6.47 | 6.38 | 5.85 | 6.62 | 6.55 | 6.12 | 6.27 | 6.93 | 6.18 | | |
| $K_2O$ | 0.02 | 0.02 | 0.02 | 0.02 | 0.08 | 0.03 | 0.02 | 0.02 | 0.03 | 0.06 | 0.02 | 0.03 | 0.08 | 0.06 | 0.03 | 0.06 | | |
| $Na_2O$ | 0.37 | 0.33 | 0.38 | 0.41 | 0.26 | 0.47 | 0.48 | 0.46 | 0.47 | 0.24 | 0.47 | 0.50 | 0.27 | 0.21 | 0.52 | 0.30 | | |
| LOI | 7.60 | 9.24 | 8.32 | 6.96 | 8.23 | 7.14 | 7.33 | 7.39 | 7.22 | 7.76 | 7.34 | 7.15 | 7.94 | 7.35 | 6.96 | 6.84 | | |
| Mg-number | 84.5 | 84.2 | 85.9 | 86.6 | 85.4 | 86.2 | 85.9 | 86.1 | 86.0 | 85.6 | 86.4 | 86.5 | 85.1 | 86.8 | 86.9 | 85.9 | | |
| P | 38.74 | 46.98 | 22.75 | 38.51 | n.d. | 45.00 | 37.56 | 44.02 | 47.17 | n.d. | 43.99 | 45.00 | n.d. | n.d. | 47.07 | n.d. | n.d. | n.d. |
| Cr | 2648 | 2642 | 3120 | 2110 | 5748 | 1688 | 3058 | 1818 | 1892 | 5589 | 1583 | 2050 | 4534 | 5597 | 1747 | 5764 | 5726 | 5216 |
| Co | 125 | 124 | 107 | 85 | 106 | 75 | 102 | 90 | 91 | 102 | 88 | 89 | 103 | 92 | 81 | 96 | 101 | 92 |
| Ni | 1949 | 1777 | 1700 | 1716 | 1830 | 1493 | 1618 | 1441 | 1447 | 1799 | 1426 | 1461 | 1999 | 1835 | 1334 | 1720 | 1616 | 1370 |
| Rb | 0.52 | 0.74 | 0.60 | 0.93 | 0.71 | 0.89 | 0.62 | 0.49 | 0.57 | 0.72 | 0.61 | 0.77 | 0.61 | 1.63 | 0.90 | 0.69 | 0.77 | 0.46 |
| Sr | 16.4 | 19.1 | 24.8 | 18.6 | 21.8 | 18.4 | 20.1 | 17.4 | 17.9 | 23.5 | 18.2 | 19.4 | 20.4 | 24.2 | 20.1 | 18.2 | 13.3 | 19.9 |
| Cs | 0.25 | 0.36 | 0.37 | 0.37 | 4.77 | 0.39 | 0.28 | 0.24 | 0.30 | 0.41 | 0.25 | 0.33 | 0.23 | 0.62 | 0.39 | 0.24 | 5.08 | 0.16 |
| Ba | 6 | 2 | 3 | 3 | 77 | 4 | 3 | 2 | 2 | 16 | 1 | 15 | 20 | 5 | 2 | 10 | 64 | 10 |
| Sc | 15 | n.d. | 10 | 25 | n.d. | 13 | 20 | 19 | 20 | n.d. | 8 | 33 | n.d. | n.d. | 13 | n.d. | n.d. | n.d. |
| V | 106 | 103 | 127 | 132 | 150 | 110 | 125 | 92 | 94 | 155 | 98 | 111 | 98 | 142 | 113 | 142 | 122 | 146 |
| Ta | 0.01 | 0.02 | 0.02 | 0.02 | 0.01 | 0.02 | 0.02 | 0.02 | 0.02 | 0.01 | 0.02 | 0.02 | 0.01 | 0.02 | 0.02 | 0.02 | 0.02 | 0.01 |
| Nb | 0.19 | 0.20 | 0.24 | 0.26 | 0.24 | 0.22 | 0.22 | 0.19 | 0.19 | 0.25 | 0.20 | 0.23 | 0.22 | 0.27 | 0.24 | 0.27 | 0.24 | 0.23 |
| Zr | 5.73 | 6.55 | 8.67 | 8.56 | 4.60 | 8.57 | 7.51 | 8.59 | 8.58 | 5.66 | 7.51 | 8.57 | 5.40 | 6.17 | 9.63 | 5.61 | 6.70 | 5.38 |
| Th | 0.03 | 0.03 | 0.04 | | 0.04 | 0.05 | 0.05 | 0.04 | 0.03 | 0.05 | 0.05 | 0.05 | 0.02 | 0.04 | 0.04 | 0.04 | 0.04 | 0.02 |
| U | 0.15 | 0.02 | 0.02 | 0.02 | 0.02 | 0.03 | 0.02 | 0.02 | 0.02 | 0.02 | 0.02 | 0.09 | 0.10 | 0.02 | 0.02 | 0.03 | 0.06 | 0.02 |
| Y | 3.75 | 3.47 | 4.04 | 4.29 | 3.71 | 3.73 | 4.34 | 3.60 | 3.65 | 4.01 | 3.85 | 3.89 | 3.48 | 4.47 | 4.04 | 4.12 | 3.21 | 3.77 |
| Cu | 15.2 | 7.1 | 7.3 | 5.2 | 6.2 | 5.3 | 5.1 | 5.2 | 4.3 | 4.8 | 4.5 | 4.8 | 6.5 | 3.8 | 4.4 | 4.7 | 4.8 | 5.1 |
| Zn | 71 | 68 | 76 | 60 | 77 | 45 | 62 | 44 | 43 | 71 | 41 | 45 | 78 | 71 | 44 | 69 | 77 | 64 |
| Mo | 0.32 | 0.08 | 0.20 | 0.56 | 0.12 | 0.35 | 0.30 | 0.26 | 0.22 | 0.14 | 0.23 | 0.34 | 3.84 | 0.96 | 0.36 | 0.26 | 0.34 | 0.22 |
| Pb | 3.48 | 2.42 | 2.07 | 14.22 | 1.47 | 6.22 | 3.33 | 3.56 | 1.62 | 1.38 | 1.63 | 9.49 | 1.39 | 1.28 | 8.30 | 2.61 | 2.28 | 0.98 |
| Bi | 0.55 | 0.43 | 0.28 | 0.93 | 0.34 | 1.05 | 0.38 | 0.99 | 1.00 | 0.29 | 0.98 | 1.04 | 0.37 | 0.22 | 1.01 | 0.35 | 0.28 | 0.39 |
| Li | 7.98 | 6.32 | 4.80 | 7.15 | 5.14 | 7.13 | 7.80 | 6.77 | 7.03 | 5.14 | 6.70 | 6.83 | 6.93 | 7.65 | 6.79 | 7.23 | 5.82 | 8.41 |
| La | 0.31 | 0.34 | 0.30 | 0.36 | 0.29 | 0.35 | 0.35 | 0.32 | 0.33 | 0.33 | 0.34 | 0.36 | 0.25 | 0.30 | 0.37 | 0.37 | 0.25 | 0.33 |
| Ce | 0.83 | 0.95 | 0.82 | 1.01 | 0.82 | 0.94 | 0.97 | 0.91 | 0.90 | 0.89 | 0.95 | 0.98 | 0.68 | 0.87 | 1.03 | 1.05 | 0.74 | 0.98 |
| Pr | 0.13 | 0.15 | 0.14 | 0.16 | 0.12 | 0.16 | 0.17 | 0.15 | 0.16 | 0.14 | 0.16 | 0.17 | 0.11 | 0.15 | 0.17 | 0.15 | 0.11 | 0.15 |
| Nd | 0.73 | 0.81 | 0.81 | 0.90 | 0.69 | 0.85 | 0.92 | 0.84 | 0.83 | 0.74 | 0.89 | 0.92 | 0.60 | 0.81 | 0.94 | 0.82 | 0.60 | 0.83 |
| Sm | 0.31 | 0.33 | 0.32 | 0.35 | 0.27 | 0.34 | 0.38 | 0.32 | 0.34 | 0.29 | 0.35 | 0.36 | 0.24 | 0.31 | 0.38 | 0.32 | 0.23 | 0.31 |

| | | | | | | | | | | | | | | | | | | |
|---|---|---|---|---|---|---|---|---|---|---|---|---|---|---|---|---|---|---|
| Eu | 0.12 | 0.13 | 0.12 | 0.14 | 0.12 | 0.15 | 0.14 | 0.15 | 0.15 | 0.12 | 0.14 | 0.16 | 0.13 | 0.13 | 0.15 | 0.14 | 0.11 | 0.14 |
| Gd | 0.47 | 0.50 | 0.50 | 0.53 | 0.47 | 0.55 | 0.57 | 0.54 | 0.55 | 0.51 | 0.54 | 0.59 | 0.43 | 0.58 | 0.61 | 0.53 | 0.41 | 0.52 |
| Tb | 0.09 | 0.09 | 0.10 | 0.11 | 0.09 | 0.10 | 0.11 | 0.10 | 0.10 | 0.10 | 0.10 | 0.11 | 0.08 | 0.11 | 0.12 | 0.10 | 0.08 | 0.10 |
| Dy | 0.67 | 0.62 | 0.69 | 0.75 | 0.62 | 0.73 | 0.76 | 0.68 | 0.73 | 0.69 | 0.73 | 0.78 | 0.59 | 0.76 | 0.79 | 0.73 | 0.58 | 0.65 |
| Ho | 0.14 | 0.13 | 0.15 | 0.17 | 0.14 | 0.16 | 0.17 | 0.15 | 0.16 | 0.15 | 0.16 | 0.17 | 0.13 | 0.17 | 0.18 | 0.16 | 0.12 | 0.15 |
| Er | 0.45 | 0.41 | 0.52 | 0.52 | 0.42 | 0.49 | 0.53 | 0.47 | 0.47 | 0.44 | 0.51 | 0.52 | 0.39 | 0.50 | 0.54 | 0.47 | 0.36 | 0.40 |
| Tm | 0.07 | 0.06 | 0.07 | 0.08 | 0.06 | 0.07 | 0.07 | 0.07 | 0.07 | 0.06 | 0.07 | 0.08 | 0.06 | 0.07 | 0.08 | 0.07 | 0.05 | 0.06 |
| Yb | 0.45 | 0.42 | 0.51 | 0.52 | 0.42 | 0.50 | 0.52 | 0.47 | 0.49 | 0.45 | 0.49 | 0.51 | 0.36 | 0.50 | 0.53 | 0.46 | 0.36 | 0.39 |
| Lu | 0.07 | 0.06 | 0.07 | 0.08 | 0.07 | 0.07 | 0.08 | 0.07 | 0.07 | 0.07 | 0.07 | 0.08 | 0.05 | 0.08 | 0.08 | 0.07 | 0.06 | 0.06 |
| $La/Yb_{cn}$ | 0.49 | 0.58 | 0.42 | 0.50 | 0.49 | 0.50 | 0.49 | 0.48 | 0.48 | 0.52 | 0.50 | 0.51 | 0.49 | 0.43 | 0.50 | 0.58 | 0.51 | 0.61 |
| $La/Sm_{cn}$ | 0.65 | 0.67 | 0.61 | 0.68 | 0.69 | 0.67 | 0.61 | 0.64 | 0.62 | 0.73 | 0.63 | 0.65 | 0.67 | 0.63 | 0.63 | 0.75 | 0.71 | 0.70 |
| $Gd/Yb_{cn}$ | 0.87 | 0.98 | 0.83 | 0.84 | 0.92 | 0.90 | 0.91 | 0.95 | 0.94 | 0.94 | 0.91 | 0.97 | 0.98 | 0.96 | 0.96 | 0.95 | 0.94 | 1.10 |
| Eu/Eu* | 0.98 | 0.99 | 0.95 | 1.01 | 1.01 | 1.05 | 0.94 | 1.07 | 1.04 | 0.98 | 1.01 | 1.08 | 1.19 | 0.91 | 0.99 | 1.03 | 1.07 | 1.09 |
| Ce/Ce* | 1.00 | 1.04 | 0.98 | 1.01 | 1.07 | 0.98 | 0.97 | 1.01 | 0.98 | 1.03 | 0.98 | 0.99 | 0.99 | 1.02 | 1.00 | 1.08 | 1.07 | 1.07 |
| $Al_2O_3/TiO_2$ | 25 | 25 | 26 | 25 | 27 | 24 | 24 | 24 | 25 | 25 | 25 | 23 | 24 | 26 | 24 | 26 | | |
| $CaO/Al_2O_3$ | 1.25 | 1.18 | 1.10 | 1.05 | 1.10 | 1.20 | 1.27 | 1.32 | 1.25 | 1.25 | 1.33 | 1.21 | 1.80 | 1.26 | 1.22 | 1.25 | | |
| Zr/Y | 1.53 | 1.89 | 2.15 | 1.99 | 1.24 | 2.30 | 1.73 | 2.39 | 2.35 | 1.41 | 1.95 | 2.20 | 1.55 | 1.38 | 2.38 | 1.36 | 2.09 | 1.43 |
| Ti/Zr | 169 | 150 | 135 | 158 | 228 | 150 | 162 | 142 | 142 | 194 | 162 | 165 | 158 | 188 | 147 | 205 | | |
| Ti/V | 9.17 | 9.54 | 9.25 | 10.24 | 7.00 | 11.68 | 9.75 | 13.22 | 12.99 | 7.06 | 12.39 | 12.73 | 8.71 | 8.15 | 12.49 | 8.11 | | |
| Ti/Ti* | 1.05 | 1.00 | 1.20 | 1.29 | 1.21 | 1.22 | 1.08 | 1.20 | 1.15 | 1.18 | 1.15 | 1.26 | 1.09 | 1.12 | 1.21 | 1.14 | | |
| Nb/Ta | 16.2 | 13.4 | 12.8 | 13.0 | 16.7 | 12.1 | 12.1 | 11.6 | 11.4 | 17.2 | 10.9 | 14.3 | 18.0 | 16.7 | 12.9 | 15.2 | 14.4 | 15.7 |
| Y/Ho | 26.5 | 25.9 | 26.4 | 25.3 | 26.1 | 23.6 | 25.5 | 23.4 | 23.0 | 26.2 | 23.8 | 23.2 | 25.9 | 25.7 | 22.2 | 25.7 | 26.2 | 25.9 |
| $Nb/La_{pm}$ | 0.63 | 0.59 | 0.79 | 0.72 | 0.83 | 0.61 | 0.63 | 0.59 | 0.59 | 0.78 | 0.57 | 0.62 | 0.86 | 0.89 | 0.65 | 0.71 | 0.93 | 0.69 |
| $Nb/Th_{pm}$ | 0.99 | 0.95 | 0.89 | | 0.84 | 0.59 | 0.55 | 0.69 | 0.81 | 0.74 | 0.54 | 0.56 | 1.20 | 0.82 | 0.75 | 0.82 | 0.75 | 1.35 |
| Nb/Nb* | 0.79 | 0.75 | 0.84 | | 0.84 | 0.60 | 0.59 | 0.63 | 0.69 | 0.76 | 0.56 | 0.59 | 1.02 | 0.86 | 0.70 | 0.76 | 0.83 | 0.96 |
| $Zr/Sm_{pm}$ | 0.75 | 0.79 | 1.09 | 0.98 | 0.68 | 1.00 | 0.79 | 1.07 | 1.00 | 0.78 | 0.86 | 0.95 | 0.89 | 0.80 | 1.02 | 0.69 | 1.15 | 0.70 |
| East | | | | | 118°.11.28′ | | | | | 118°.11.28′ | | | 118°.11.23′ | 118°.11.28′ | | 118°.11.24′ | | |
| North | | | | | 35°.46.52′ | | | | | 35°.46.52′ | | | 35°.46.53′ | 35°.46.52′ | | 35°.46.48′ | | |

Samples were recalculated to 100% anhydrous for inter-comparisons. Mg-numbers are calculated as the molecular ratio of $Mg/(Mg+Fe^{2+})$, where $Fe^{2+}$ is assumed to be 90% of total Fe. Nb/Nb*, Ce/Ce* and Eu/Eu* ratios were calculated with respect to the neighbouring immobile elements, following the method of Taylor and McLennan (1985). *Samples with strong alteration.
n.d.: not determined. Sample locations are given by East and North readings in Global Positioning System (GPS).

versus 17.9–19.1 wt.%) values than spinifex counterparts, resulting in higher forsterite ($Fo_{86.6–86.9}$ versus $Fo_{82.0–83.8}$) values for the former group. The cumulate olivines, however, have higher $SiO_2$ (39.7–39.9 versus 38.8–39.4 wt.%) than spinifex counterparts. Olivines in the Taishan komatiites have lower Fo values than those in most Archean komatiites but are comparable to metamorphic olivines of the 2.7 Ga Sula Mountain komatiites (Table 5; see Renner et al., 1994; Rollinson, 1999).

### 5.3. Nd isotopes

The Sm–Nd isotope data for the Taishan komatiites yield an errorchron age of 2712±740 Ma (MSWD=59) [Fig. 9b; Table 6; excluding two outliers KM3B, KM4]. This age, within uncertainties, is in agreement with whole-rock Sm–Nd and Rb–Sr isochron ages of spatially associated mafic volcanic and intrusive rocks (see Jahn et al., 1988; Cao et al., 1996). Using a least square fitting routine (Ludwig,

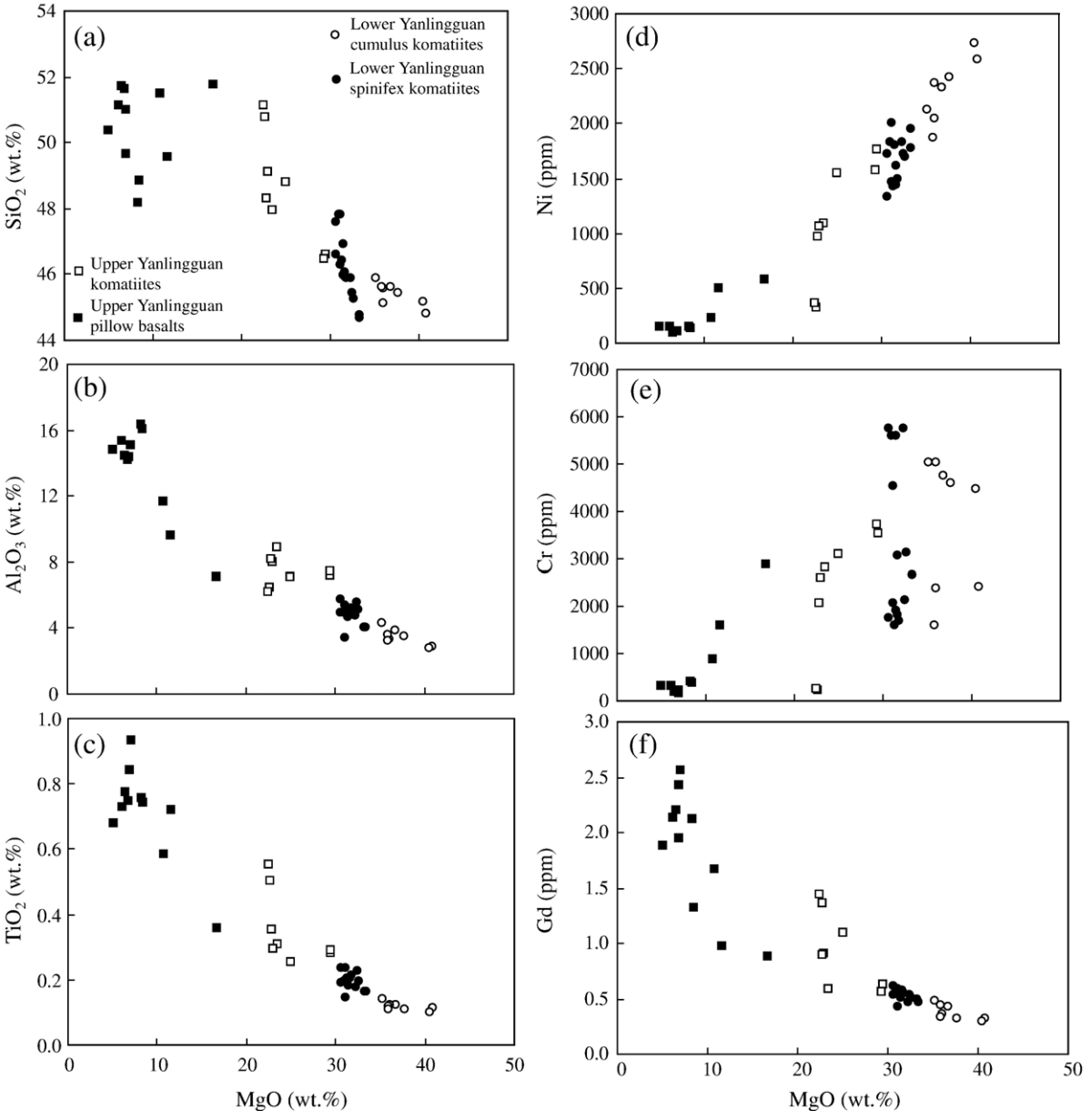


Fig. 6. MgO (wt.%) versus selected element variation diagrams for komatiites and pillow basalts. Trends in some plots unlikely to reflect the olivine fractionation path, rather they point towards serpentine and/or chlorite (cf. Parman et al., 1997).

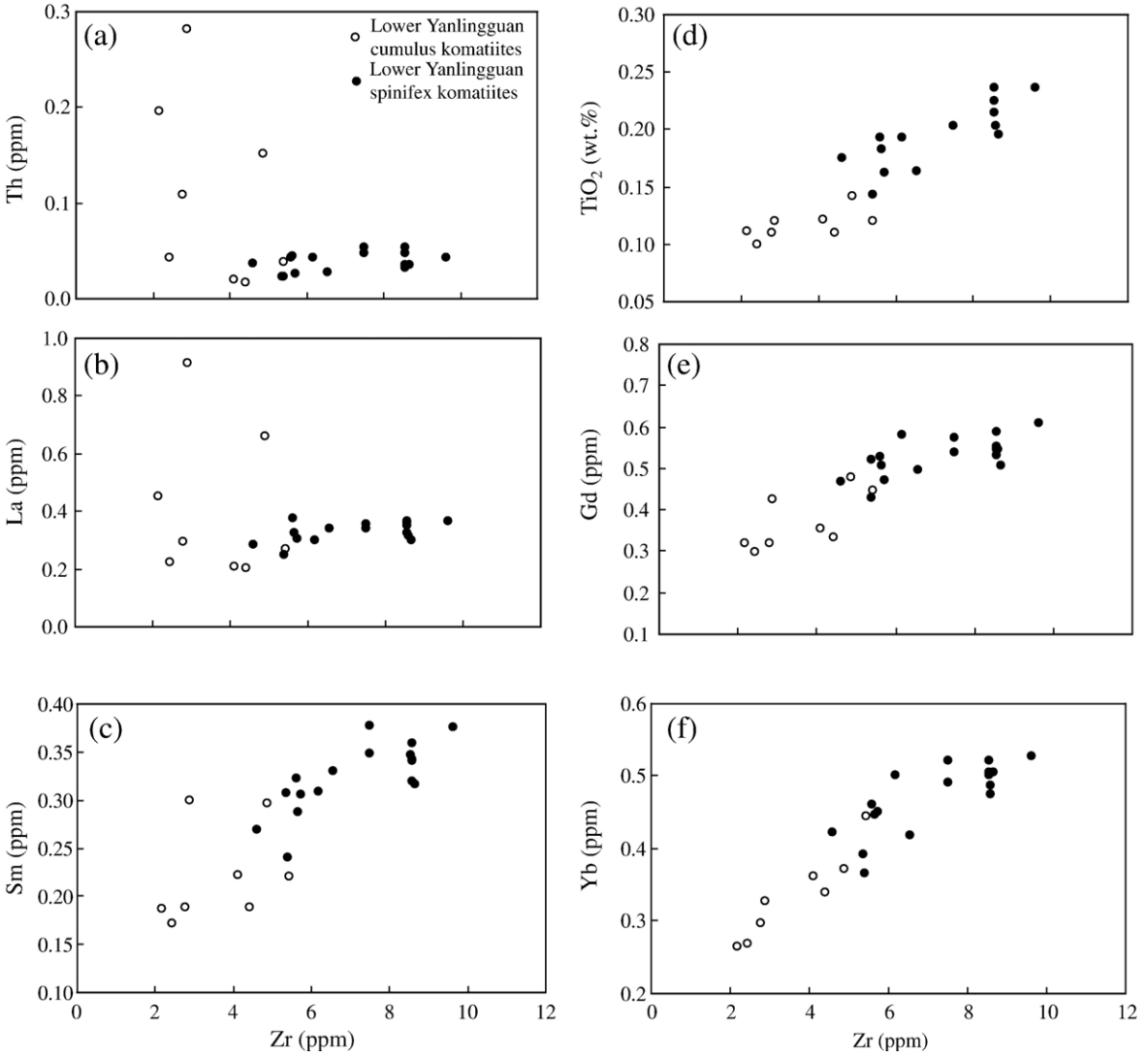


Fig. 7. Zr (ppm) versus selected element variation diagrams for komatiites in the Lower Yanlingguan Formation. Large variations in highly incompatible elements (e.g. Th, La, Nd) are likely to have resulted from crustal contamination.

2001), we regressed the Sm–Nd data for spatially associated metabasalts (see Jahn et al., 1988), and obtained an age of 2704±90 Ma (MSWD=11). Because of its smaller error and MSWD value, the latter age (2704±90 Ma) is used to calculate the initial $\varepsilon_{Nd}$ values of the Taishan komatiites. Although this age is likely to reflect the age of metamorphism rather than the age of eruption, it can reliably be used to calculate the initial $\varepsilon_{Nd}$ values of komatiites because both komatiites and basalts underwent regional metamorphism shortly after their eruption (Cao et al., 1996; Zhang et al., 2001). Notwithstanding the coherent immobile trace element variations komatiites display a relatively large range of initial $\varepsilon_{Nd}$ (−0.4 to +3.6) values.

## 6. Discussion

### 6.1. Origin of olivines

In the cumulate layers olivine grains are enclosed in a matrix of serpentine (Fig. 5e, f). These olivines have lower Mg-numbers ($Fo_{83.9–84.3}$) values than the whole-rock (88) composition (Tables 3 and 5). Olivines in the spinifex layers occur in a serpentine–chlorite–amphibolite matrix (Fig. 5c, d; Table 7).

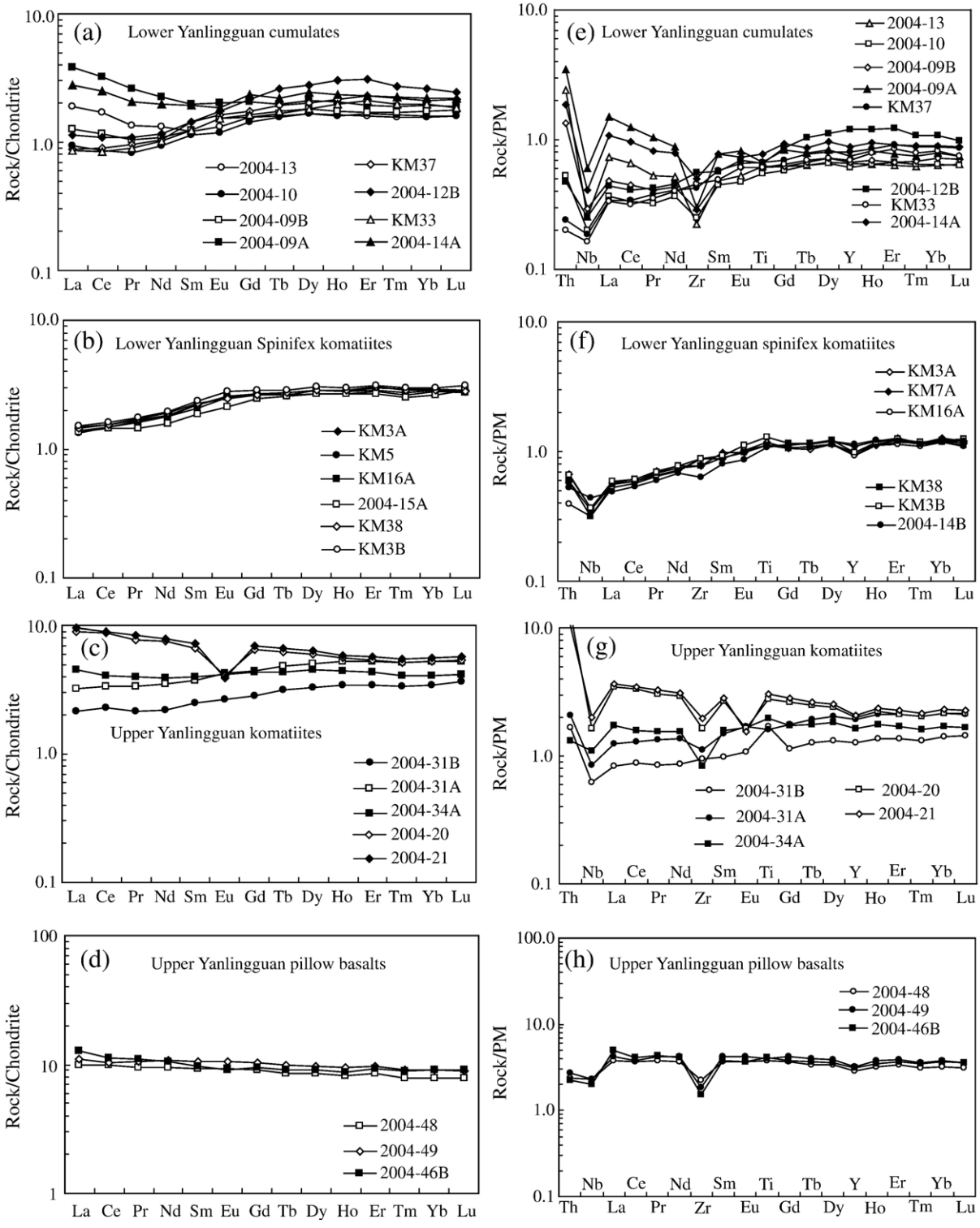


Fig. 8. Chondrite- and primitive mantle-normalized patterns for komatiites and pillow basalts. Chondrite and primitive mantle normalization values are from Sun and McDonough (1989), and from Hofmann (1988), respectively.

These olivines also display lower Mg-numbers ($Fo_{78.6–80.8}$) than the whole-rock (84–87) and matrix (90–95) compositions (Tables 3, 5, and 7). These results indicate that olivines are not in equilibrium with the whole-rock composition of komatiites. Rather, it is likely that olivines became more Fe-rich during metamorphic recrystallization, resulting in lower Mg/Fe ratios (cf. Arndt, 1994; Renner et al., 1994; Rollinson, 1999).

### 6.2. Geochemical effects of alteration

Given that all samples analysed for this study have been altered to some extent, we use the terms "least-altered" and "strongly-altered" to define near-primary and significantly modified geochemical signatures, respectively (Tables 3 and 4). Following Polat and Hofmann (2003), samples having significant carbonate and silica replacement (>2%) or large Ce anomalies (Ce/Ce*>1.1 and Ce/Ce*<0.9) are considered as "strongly altered" (Tables 3 and 4).

The abundances of Si, Ca, Fe, P, Pb, U, Cr, Co, and LILE in the Taishan komatiites show relatively large variations, which do not correlate well with Zr abundances, and show weak correlations with MgO and Ni contents (Fig. 6). Thus, the large concentration variations of these elements in the Taishan komatiites likely signify loss or gain of these elements during post-magmatic alteration (Tables 3 and 4).

On diagrams of MgO, Zr, and Sm versus REE, HFSE, and Ni most samples display systematic variations, consistent with limited mobility of these elements during alteration. Highly incompatible elements display larger spread than the moderately incompatible to compatible elements on MgO, Zr, and Sm diagrams (Figs. 6 and 7).

All lower komatiites have coherent REE patterns, without significant Ce or Eu anomalies, consistent with limited mobility of REE during post-magmatic alteration (Fig. 8; Table 3). In contrast, some samples from the upper Yanlingguan Formation, with significant carbonate replacement (2–6%), display large Ce anomalies (Ce/Ce*=0.85–1.30), consistent with mobility of REE (Fig. 9c; Table 4). Carbonate alteration is more pronounced in pillow basalts as manifested by 1–15-cm thick calcite veins. Pillow basalts having more than 4% carbonate replacement display convex-up REE patterns (Fig. 9d). Many of these flows do not have large Ce anomalies; however they have been classified as "strongly altered" given modal carbonate >4%. Convex-upward patterns likely resulted from loss of LREE during carbonate alteration (cf. Polat and Hofmann, 2003). The intensity of carbonate alteration increases toward shear zones, suggesting that these acted as conduits for the migration of carbonate-rich fluids.

The large spread in the initial $\varepsilon_{Nd}$ values (−0.4 to +3.6) could possibly reflect metasomatic alteration. However, post-magmatic metasomatic alteration is unlikely to have caused variable initial $\varepsilon_{Nd}$ in the Taishan komatiites given: (1) both Sm and Nd appear to have been immobile; and (2) there are no co-variations between $\varepsilon_{Nd}$ (and Sm/Nd), or mobile elements (e.g. K, Ba, Pb, P), or Mg-numbers in olivines.

### 6.3. Crustal contamination

Older basement rocks are not exposed beneath the Taishan greenstone belt. However, the presence of gneissic and granitic clasts in conglomerates, and zircon and apatite xenocrysts in komatiites lower in the formation (Fig. 5b; Zhang et al., 2001), signify that the Taishan volcanic-sedimentary sequence was deposited on continental basement. Similarly, the petrographic and geochemical characteristics of greywacke sandstones are consistent with a close continental source area (Fig. 9a). Therefore, it is possible that the Taishan volcanic rocks were contaminated by crust during eruption.

The Taishan komatiites possess negative Nb anomalies (Nb/Nb*=0.19–0.96) and a larger range of initial $\varepsilon_{Nd}$ values (−0.4 to +3.6) than Wawa or Baltic counterparts (Figs. 8 and 10; Tables 3–5). The magnitude of Nb anomalies correlates well with $\varepsilon_{Nd}$ values, consistent with variable degrees of contamination by older continental rocks (Figs. 8 and 10).

Three possible processes of crustal contamination might have taken place during or prior to the emplacement of the komatiites: (1) assimilation of sandstones, andesites and rhyolites, like those that are exposed in the upper Yanlingguan and Shancaoyu Formations (cf. Barrie, 1999; Wyman et al., 1999); (2) the mantle source region may have been contaminated by older recycled sediments if the komatiite melts originated from a metasomatized sub-arc mantle wedge (cf. Parman et al., 2001, 2003); or (3) they may have interacted with older continental basement during their ascent (Sun et al., 1989). Sandstones, andesites, and rhyolites are stratigraphically located at the upper levels in the Taishan belt (Fig. 3), suggesting that the first

Table 4
Major and trace element concentrations and selected element ratios for komatiites and pillow basalts in the upper Yanlingguan Formation*

| | Komatiites | | | | | | | | Pillow basalts–amphibolites | | | | |
|---|---|---|---|---|---|---|---|---|---|---|---|---|---|
| | 2004-31B | 2004-31A | 2004-34A | 2004-20 | 2004-21 | 2004-29A* | 2004-30* | 2004-28* | 2004-48 | 2004-49 | 2004-46B | 2004-25* | 2004-19* |
| $SiO_2$ | 47.95 | 49.12 | 48.32 | 50.77 | 51.12 | 46.61 | 46.48 | 48.78 | 50.36 | 51.13 | 51.63 | 49.57 | 51.49 |
| $TiO_2$ | 0.31 | 0.29 | 0.35 | 0.50 | 0.55 | 0.28 | 0.29 | 0.25 | 0.68 | 0.73 | 0.75 | 0.72 | 0.58 |
| $Al_2O_3$ | 8.86 | 7.95 | 8.18 | 6.49 | 6.22 | 7.20 | 7.46 | 7.07 | 14.82 | 15.34 | 14.17 | 9.55 | 11.69 |
| $Fe_2O_3$ | 10.30 | 9.87 | 10.14 | 10.97 | 11.15 | 10.89 | 10.90 | 10.29 | 10.41 | 10.49 | 13.06 | 14.54 | 11.84 |
| MnO | 0.17 | 0.16 | 0.18 | 0.24 | 0.25 | 0.17 | 0.17 | 0.15 | 0.18 | 0.18 | 0.20 | 0.31 | 0.19 |
| MgO | 23.46 | 23.02 | 22.82 | 22.75 | 22.54 | 29.54 | 29.39 | 25.02 | 5.07 | 6.20 | 6.82 | 11.64 | 10.77 |
| CaO | 8.67 | 9.26 | 9.38 | 8.12 | 8.01 | 5.25 | 5.25 | 8.32 | 16.80 | 12.99 | 9.93 | 12.32 | 11.31 |
| $K_2O$ | 0.08 | 0.09 | 0.10 | 0.05 | 0.05 | 0.04 | 0.03 | 0.05 | 0.36 | 0.41 | 0.64 | 0.48 | 0.18 |
| $Na_2O$ | 0.18 | 0.21 | 0.50 | 0.05 | 0.05 | 0.01 | 0.01 | 0.05 | 1.26 | 2.49 | 2.74 | 0.81 | 1.90 |
| LOI | 5.32 | 4.71 | 4.38 | 4.28 | 4.11 | 7.70 | 7.58 | 5.15 | 1.21 | 0.96 | 0.70 | 2.67 | 0.70 |
| Mg-number | 81.8 | 82.2 | 81.7 | 80.4 | 80.0 | 84.3 | 84.2 | 82.8 | 49.1 | 53.9 | 50.8 | 61.3 | 64.3 |
| P | 87 | 44 | 87 | 262 | 218 | 44 | 44 | 44 | 221 | 221 | 264 | 218 | 218 |
| Cr | 2812 | 2596 | 2066 | 222 | 251 | 3532 | 3711 | 3092 | 299 | 327 | 188 | 1591 | 875 |
| Co | 112 | 107 | 111 | 95 | 97 | 162 | 151 | 130 | 40 | 49 | 57 | 93 | 54 |
| Ni | 1085 | 1057 | 973 | 323 | 366 | 1766 | 1570 | 1546 | 147 | 151 | 109 | 497 | 225 |
| Rb | 0.08 | 0.11 | 0.07 | 0.20 | 0.08 | 0.00 | 0.01 | 0.01 | 30.4 | 26.2 | 26.2 | 2.71 | 0.22 |
| Sr | 106 | 167 | 122 | 62 | 54 | 68 | 56 | 61 | 248 | 221 | 169 | 43 | 199 |
| Ba | 3.9 | 6.8 | 9.1 | 2.7 | 2.4 | 3.4 | 3.6 | 2.1 | 140 | 392 | 118 | 36.1 | 19.2 |
| V | 14.7 | 27.2 | 16.7 | 21.6 | 15.7 | 11.0 | 12.9 | 11.6 | n.d. | n.d. | n.d. | 18.9 | 25.7 |
| Ta | 0.02 | 0.03 | 0.04 | 0.07 | 0.08 | 0.02 | 0.02 | 0.01 | 0.08 | 0.09 | 0.07 | 0.03 | 0.09 |
| Nb | 0.38 | 0.52 | 0.68 | 1.02 | 1.23 | 0.38 | 0.34 | 0.22 | 1.41 | 1.41 | 1.23 | 0.39 | 1.26 |
| Zr | 9.2 | 10.8 | 8.1 | 16.0 | 19.2 | 10.0 | 8.9 | 8.3 | 21.6 | 17.9 | 15.0 | 7.2 | 28.1 |
| Th | 0.14 | 0.17 | 0.11 | 1.07 | 0.85 | 0.05 | 0.27 | 0.06 | 0.19 | 0.22 | 0.18 | 0.23 | 0.88 |
| U | 0.02 | 0.02 | 0.02 | 0.08 | 0.09 | 0.01 | 0.02 | 0.01 | 0.06 | 0.04 | 0.04 | 0.03 | 0.12 |
| Y | 5.0 | 7.6 | 6.5 | 7.9 | 8.3 | 4.8 | 4.3 | 7.7 | 11 | 13 | 12 | 5.7 | 11.1 |
| Cu | 17 | 26 | 2 | 20 | 10 | 11 | 12 | 3 | 64 | 27 | 53 | 29 | 27 |
| Zn | 16 | 23 | 26 | 25 | 21 | 21 | 22 | 16 | 27 | 37 | 35 | 13 | 24 |
| Mo | 0.18 | 0.09 | 0.10 | 0.09 | 0.08 | 0.06 | 0.09 | 0.07 | 1.69 | 0.20 | 0.11 | 0.10 | 0.08 |
| Pb | 0.26 | 0.24 | 0.13 | 0.56 | 0.30 | 0.27 | 0.46 | 0.207 | 2.57 | 2.80 | 1.28 | 0.38 | 0.63 |
| Bi | 0.30 | 0.45 | 0.09 | 0.13 | 0.13 | 0.68 | 0.63 | 0.151 | 0.76 | 0.63 | 0.16 | 0.13 | 0.04 |
| Li | 13.61 | 15.52 | 12.73 | 9.18 | 8.43 | 0.71 | 0.41 | 0.871 | 19.51 | 13.04 | 11.30 | 17.43 | 23.63 |

| | | | | | | | | | | | | | |
|---|---|---|---|---|---|---|---|---|---|---|---|---|---|
| La | 0.52 | 0.77 | 1.07 | 2.13 | 2.26 | 0.58 | 0.66 | 0.84 | 2.35 | 2.60 | 3.05 | 0.85 | 2.72 |
| Ce | 1.41 | 2.08 | 2.51 | 5.34 | 5.52 | 1.25 | 2.19 | 2.73 | 6.09 | 6.30 | 6.91 | 2.18 | 6.15 |
| Pr | 0.21 | 0.32 | 0.38 | 0.74 | 0.80 | 0.22 | 0.25 | 0.46 | 0.91 | 1.01 | 1.04 | 0.34 | 0.83 |
| Nd | 1.03 | 1.63 | 1.83 | 3.52 | 3.72 | 1.16 | 1.20 | 2.44 | 4.43 | 5.01 | 4.91 | 1.73 | 3.75 |
| Sm | 0.38 | 0.58 | 0.61 | 1.03 | 1.10 | 0.41 | 0.39 | 0.78 | 1.43 | 1.62 | 1.47 | 0.65 | 1.15 |
| Eu | 0.16 | 0.25 | 0.24 | 0.24 | 0.23 | 0.11 | 0.11 | 0.25 | 0.53 | 0.61 | 0.53 | 0.26 | 0.43 |
| Gd | 0.58 | 0.91 | 0.90 | 1.36 | 1.44 | 0.62 | 0.56 | 1.09 | 1.88 | 2.14 | 1.94 | 0.98 | 1.67 |
| Tb | 0.12 | 0.18 | 0.16 | 0.23 | 0.25 | 0.12 | 0.10 | 0.19 | 0.32 | 0.37 | 0.34 | 0.17 | 0.30 |
| Dy | 0.83 | 1.29 | 1.16 | 1.52 | 1.62 | 0.81 | 0.74 | 1.34 | 2.16 | 2.48 | 2.30 | 1.13 | 2.03 |
| Ho | 0.20 | 0.30 | 0.25 | 0.32 | 0.34 | 0.18 | 0.16 | 0.30 | 0.46 | 0.53 | 0.49 | 0.23 | 0.43 |
| Er | 0.57 | 0.88 | 0.71 | 0.89 | 0.94 | 0.53 | 0.49 | 0.86 | 1.42 | 1.61 | 1.55 | 0.61 | 1.22 |
| Tm | 0.09 | 0.13 | 0.10 | 0.13 | 0.14 | 0.08 | 0.07 | 0.13 | 0.20 | 0.23 | 0.22 | 0.08 | 0.18 |
| Yb | 0.59 | 0.90 | 0.70 | 0.89 | 0.96 | 0.53 | 0.48 | 0.83 | 1.34 | 1.55 | 1.53 | 0.51 | 1.14 |
| Lu | 0.09 | 0.13 | 0.11 | 0.14 | 0.15 | 0.08 | 0.07 | 0.13 | 0.20 | 0.23 | 0.23 | 0.07 | 0.17 |
| $La/Yb_{cn}$ | 0.63 | 0.61 | 1.09 | 1.71 | 1.70 | 0.78 | 1.00 | 0.72 | 1.26 | 1.20 | 1.42 | 1.19 | 1.71 |
| $La/Sm_{cn}$ | 0.87 | 0.85 | 1.13 | 1.34 | 1.33 | 0.91 | 1.09 | 0.69 | 1.18 | 1.15 | 1.48 | 0.85 | 1.52 |
| $Gd/Yb_{cn}$ | 0.82 | 0.84 | 1.06 | 1.26 | 1.25 | 0.97 | 0.98 | 1.08 | 1.16 | 1.14 | 1.05 | 1.58 | 1.21 |
| Eu/Eu* | 1.01 | 1.04 | 1.01 | 0.61 | 0.55 | 0.68 | 0.74 | 0.82 | 1.00 | 1.01 | 0.96 | 1.00 | 0.95 |
| Ce/Ce* | 1.06 | 1.02 | 0.97 | 1.04 | 1.01 | 0.85 | 1.32 | 1.07 | 0.97 | 0.90 | 0.90 | 1.00 | 1.00 |
| $Al_2O_3/TiO_2$ | 29 | 27 | 23 | 13 | 11 | 26 | 26 | 28 | 22 | 21 | 19 | 13 | 20 |
| $CaO/Al_2O_3$ | 0.98 | 1.16 | 1.15 | 1.25 | 1.29 | 0.73 | 0.70 | 1.18 | 1.13 | 0.85 | 0.70 | 1.29 | 0.97 |
| Zr/Y | 1.86 | 1.42 | 1.25 | 2.02 | 2.32 | 2.10 | 2.07 | 1.08 | 1.91 | 1.40 | 1.21 | 1.26 | 2.53 |
| Ti/Zr | 198 | 163 | 263 | 188 | 172 | 168 | 196 | 184 | 188 | 243 | 299 | 596 | 125 |
| Ti/Ti* | 1.59 | 0.99 | 1.18 | 1.04 | 1.07 | 1.36 | 1.52 | 0.68 | 0.98 | 0.93 | 1.04 | 2.23 | 1.04 |
| Nb/Ta | 16.8 | 17.7 | 17.8 | 14.7 | 15.0 | 17.5 | 16.8 | 17.6 | 18.5 | 16.5 | 17.0 | 14.7 | 14.8 |
| Y/Ho | 25.3 | 25.4 | 25.6 | 24.9 | 24.6 | 26.2 | 26.3 | 26.0 | 24.6 | 24.0 | 25.1 | 24.8 | 25.7 |
| $Nb/La_{pm}$ | 0.74 | 0.68 | 0.63 | 0.47 | 0.54 | 0.66 | 0.52 | 0.25 | 0.60 | 0.54 | 0.40 | 0.46 | 0.46 |
| $Nb/Th_{pm}$ | 0.37 | 0.40 | 0.83 | 0.12 | 0.19 | 1.03 | 0.17 | 0.45 | 0.97 | 0.84 | 0.89 | 0.22 | 0.19 |
| Nb/Nb* | 0.52 | 0.52 | 0.73 | 0.24 | 0.32 | 0.82 | 0.30 | 0.34 | 0.76 | 0.67 | 0.60 | 0.32 | 0.29 |
| $Zr/Sm_{pm}$ | 0.96 | 0.74 | 0.53 | 0.62 | 0.69 | 0.97 | 0.90 | 0.42 | 0.60 | 0.44 | 0.40 | 0.45 | 0.97 |
| East | 117°.36.26′ | 117°.36.24′ | 117°.01.74′ | 117°.34.16′ | 117°.34.16′ | 117°.36.26′ | 117°.36.26′ | 117°.36.16′ | 117°.28.04′ | 117°.28.04′ | 117°.27.95′ | 117°.35.97′ | 117°.34.26′ |
| North | 36°.02.02′ | 36°.02.04′ | 36°.02.04′ | 36°.03.66′ | 36°.03.66′ | 36°.02.02′ | 36°.02.02′ | 36°.02.12′ | 36°.25.39′ | 36°.25.39′ | 36°.25.70′ | 36°.02.07′ | 36°.03.67′ |

*(continued on next page)*

Table 4 (*continued*)

| | Pillow basalts–amphibolites | | | | | | Sandstones | | | |
|---|---|---|---|---|---|---|---|---|---|---|
| | 2004-26* | 2004-27* | 2004-24* | 2004-22* | 2004-43* | 2004-46A* | 2004-35 | 2004-36 | 2004-37 | Average sandstone |
| $SiO_2$ | 48.86 | 48.19 | 49.65 | 51.78 | 50.99 | 51.72 | 70.36 | 71.52 | 63.14 | 68.34 |
| $TiO_2$ | 0.74 | 0.75 | 0.93 | 0.36 | 0.84 | 0.77 | 0.35 | 0.36 | 0.42 | 0.38 |
| $Al_2O_3$ | 16.05 | 16.32 | 15.07 | 7.06 | 14.38 | 14.48 | 14.93 | 14.77 | 18.24 | 15.98 |
| $Fe_2O_3$ | 12.16 | 12.55 | 13.69 | 10.27 | 13.21 | 12.96 | 3.55 | 3.39 | 4.46 | 3.80 |
| MnO | 0.17 | 0.17 | 0.21 | 0.19 | 0.22 | 0.20 | 0.04 | 0.05 | 0.06 | 0.05 |
| MgO | 8.45 | 8.33 | 7.07 | 16.76 | 6.93 | 6.50 | 1.56 | 1.02 | 1.23 | 1.27 |
| CaO | 10.42 | 10.69 | 10.72 | 12.50 | 10.90 | 9.79 | 2.79 | 2.55 | 4.12 | 3.15 |
| $K_2O$ | 0.16 | 0.17 | 0.12 | 0.30 | 0.21 | 0.67 | 2.39 | 2.89 | 2.77 | 2.68 |
| $Na_2O$ | 2.95 | 2.75 | 2.46 | 0.77 | 2.26 | 2.83 | 3.94 | 3.37 | 5.50 | 4.27 |
| LOI | 0.55 | 0.70 | 0.30 | 0.91 | 1.21 | 0.76 | 0.96 | 1.16 | 4.44 | 2.19 |
| Mg-number | 57.9 | 56.8 | 50.6 | 76.4 | 50.9 | 49.8 | 46.4 | 37.3 | 35.4 | 39.8 |
| P | 218 | 262 | 305 | n.d. | 265 | 263 | 353 | 352 | 319 | 341 |
| Cr | 384 | 394 | 220 | 2876 | 147 | 172 | 96 | 50 | 66 | 70 |
| Co | 60 | 58 | 54 | 74 | 58 | 51 | 15 | 10 | 17 | 14 |
| Ni | 137 | 144 | 102 | 581 | 108 | 97 | 36 | 14 | 27 | 26 |
| Rb | 0.05 | 0.15 | 0.13 | 1.09 | 8.1 | 36.3 | 86 | 97 | 99 | 94 |
| Sr | 217 | 344 | 150 | 313 | 126 | 224 | 440 | 660 | 482 | 527 |
| Ba | 6.7 | 10.3 | 26.1 | 17.6 | 51 | 150 | 890 | 1366 | 654 | 970 |
| V | 11.6 | 26.1 | 26.0 | 10.7 | n.d. | n.d. | n.d. | n.d. | n.d. | |
| Ta | 0.05 | 0.09 | 0.09 | 0.05 | 0.10 | 0.09 | 0.33 | 0.35 | 0.39 | 0.36 |
| Nb | 0.90 | 1.41 | 1.49 | 1.01 | 1.52 | 1.49 | 4.08 | 3.74 | 5.19 | 4.34 |
| Zr | 22.1 | 35.1 | 28.6 | 18.4 | 19.2 | 20.9 | 127.5 | 112.4 | 77.4 | 106 |
| Th | 0.14 | 0.23 | 0.75 | 0.25 | 0.20 | 0.20 | 5.96 | 7.75 | 7.71 | 7.14 |
| U | 0.02 | 0.04 | 0.41 | 0.04 | 0.03 | 0.07 | 0.60 | 0.74 | 0.54 | 0.63 |
| Y | 8.3 | 13.9 | 16.9 | 5.4 | 15 | 15 | 6.63 | 4.89 | 8.22 | 6.58 |
| Cu | 27 | 43 | 74 | 9 | 77 | 80 | 11.45 | 14.05 | 2.42 | 9.31 |
| Zn | 15 | 25 | 29 | 23 | 157 | 36 | 19 | 78 | 11 | 36 |
| Mo | 0.07 | 0.10 | 0.14 | 0.09 | 0.13 | 0.15 | 0.06 | 0.07 | 0.06 | 0.06 |
| Pb | 0.22 | 0.41 | 0.28 | 0.64 | 12.17 | 3.01 | 2.82 | 8.67 | 2.32 | 4.60 |
| Bi | 0.20 | 0.28 | 0.06 | 0.84 | 0.26 | 0.17 | 0.16 | 0.23 | 1.40 | 0.60 |
| Li | 121.21 | 177.99 | 39.84 | 11.19 | 6.41 | 17.01 | 9.91 | 8.67 | 3.97 | 7.52 |
| La | 1.15 | 1.78 | 2.63 | 1.36 | 2.59 | 4.38 | 18.65 | 12.60 | 28.06 | 19.77 |
| Ce | 3.32 | 5.42 | 6.73 | 2.81 | 5.57 | 9.07 | 37.30 | 28.08 | 58.86 | 41.41 |

| | | | | | | | | | | |
|---|---|---|---|---|---|---|---|---|---|---|
| Pr | 0.53 | 0.85 | 1.01 | 0.46 | 1.04 | 1.30 | 4.17 | 3.31 | 5.95 | 4.48 |
| Nd | 2.73 | 4.37 | 5.14 | 2.11 | 5.29 | 5.92 | 14.76 | 12.00 | 20.88 | 15.88 |
| Sm | 0.89 | 1.44 | 1.73 | 0.63 | 1.79 | 1.78 | 2.48 | 2.01 | 3.37 | 2.62 |
| Eu | 0.38 | 0.58 | 0.71 | 0.24 | 0.63 | 0.61 | 0.64 | 0.54 | 0.80 | 0.66 |
| Gd | 1.32 | 2.12 | 2.56 | 0.87 | 2.42 | 2.20 | 1.73 | 1.31 | 2.37 | 1.80 |
| Tb | 0.24 | 0.38 | 0.45 | 0.15 | 0.42 | 0.38 | 0.23 | 0.18 | 0.32 | 0.24 |
| Dy | 1.57 | 2.53 | 3.10 | 1.00 | 2.82 | 2.60 | 1.27 | 0.94 | 1.67 | 1.29 |
| Ho | 0.33 | 0.54 | 0.66 | 0.21 | 0.61 | 0.56 | 0.25 | 0.19 | 0.31 | 0.25 |
| Er | 0.91 | 1.53 | 1.86 | 0.60 | 1.85 | 1.76 | 0.78 | 0.60 | 0.95 | 0.78 |
| Tm | 0.13 | 0.22 | 0.27 | 0.09 | 0.26 | 0.26 | 0.11 | 0.08 | 0.13 | 0.11 |
| Yb | 0.89 | 1.44 | 1.75 | 0.58 | 1.78 | 1.74 | 0.76 | 0.60 | 0.83 | 0.73 |
| Lu | 0.13 | 0.22 | 0.26 | 0.09 | 0.25 | 0.26 | 0.12 | 0.09 | 0.12 | 0.11 |
| $La/Yb_{cn}$ | 0.93 | 0.89 | 1.08 | 1.67 | 1.05 | 1.80 | 17.48 | 14.98 | 24.13 | 18.87 |
| $La/Sm_{cn}$ | 0.83 | 0.80 | 0.98 | 1.39 | 1.04 | 1.76 | 5.39 | 4.49 | 5.98 | 5.28 |
| $Gd/Yb_{cn}$ | 1.23 | 1.22 | 1.21 | 1.24 | 1.13 | 1.05 | 1.87 | 1.80 | 2.35 | 2.01 |
| Eu/Eu* | 1.07 | 1.01 | 1.03 | 0.99 | 0.92 | 0.94 | 0.90 | 0.95 | 0.82 | 0.89 |
| Ce/Ce* | 1.04 | 1.08 | 1.01 | 0.87 | 0.79 | 0.88 | 0.98 | 1.01 | 1.06 | 1.02 |
| $Al_2O_3/TiO_2$ | 22 | 22 | 16 | 20 | 17 | 19 | 42 | 41 | 44 | 42 |
| $CaO/Al_2O_3$ | 0.65 | 0.66 | 0.71 | 1.77 | 0.76 | 0.68 | 0.19 | 0.17 | 0.23 | 0.20 |
| Zr/Y | 2.65 | 2.53 | 1.70 | 3.40 | 1.25 | 1.43 | 16.0 | 19.1 | 7.8 | 14.3 |
| Ti/Zr | 202 | 129 | 195 | 116 | 262 | 223 | 17 | 19 | 32 | 23 |
| Ti/Ti* | 1.69 | 1.06 | 1.09 | 1.18 | 0.96 | 0.93 | 0.34 | 0.44 | 0.29 | 0.36 |
| Nb/Ta | 16.7 | 16.6 | 16.1 | 18.8 | 15.7 | 17.0 | 12.2 | 10.8 | 13.4 | 12.1 |
| Y/Ho | 25.3 | 25.5 | 25.8 | 25.4 | 25.2 | 25.9 | 26.6 | 26.0 | 26.5 | 26.4 |
| $Nb/La_{pm}$ | 0.78 | 0.79 | 0.56 | 0.74 | 0.58 | 0.34 | 0.22 | 0.30 | 0.18 | 0.23 |
| $Nb/Th_{pm}$ | 0.83 | 0.79 | 0.26 | 0.53 | 1.02 | 0.99 | 0.09 | 0.06 | 0.09 | 0.08 |
| Nb/Nb* | 0.81 | 0.79 | 0.38 | 0.63 | 0.77 | 0.58 | 0.14 | 0.14 | 0.13 | 0.13 |
| $Zr/Sm_{pm}$ | 0.99 | 0.97 | 0.66 | 1.16 | 0.43 | 0.47 | 1.70 | 1.85 | 0.76 | 1.44 |
| East | 117°.35.97′ | 117°.35.97′ | 117°.34.37′ | 117°.34.16′ | 117°.22.79′ | 117°.27.95′ | 117°.31.79′ | 117°.31.69′ | 117°.31.90′ | |
| North | 36°.02.07′ | 36°.02.07′ | 36°.03.80′ | 36°.03.66′ | 36°.25.38′ | 36°.25.70′ | 36°.03.08′ | 36°.03.17′ | 36°.03.01′ | |

Samples were recalculated to 100% anhydrous for inter-comparisons. Mg-numbers are calculated as the molecular ratio of $Mg/(Mg+Fe^{2+})$, where $Fe^{2+}$ is assumed to be 90% of total Fe. Nb/Nb*, Ce/Ce* and Eu/Eu* ratios were calculated with respect to the neighbouring immobile elements, following the method of Taylor and McLennan (1985). *Samples with strong alteration. n.d.: not determined. Sample locations are given by East and North readings in Global Positioning System (GPS).

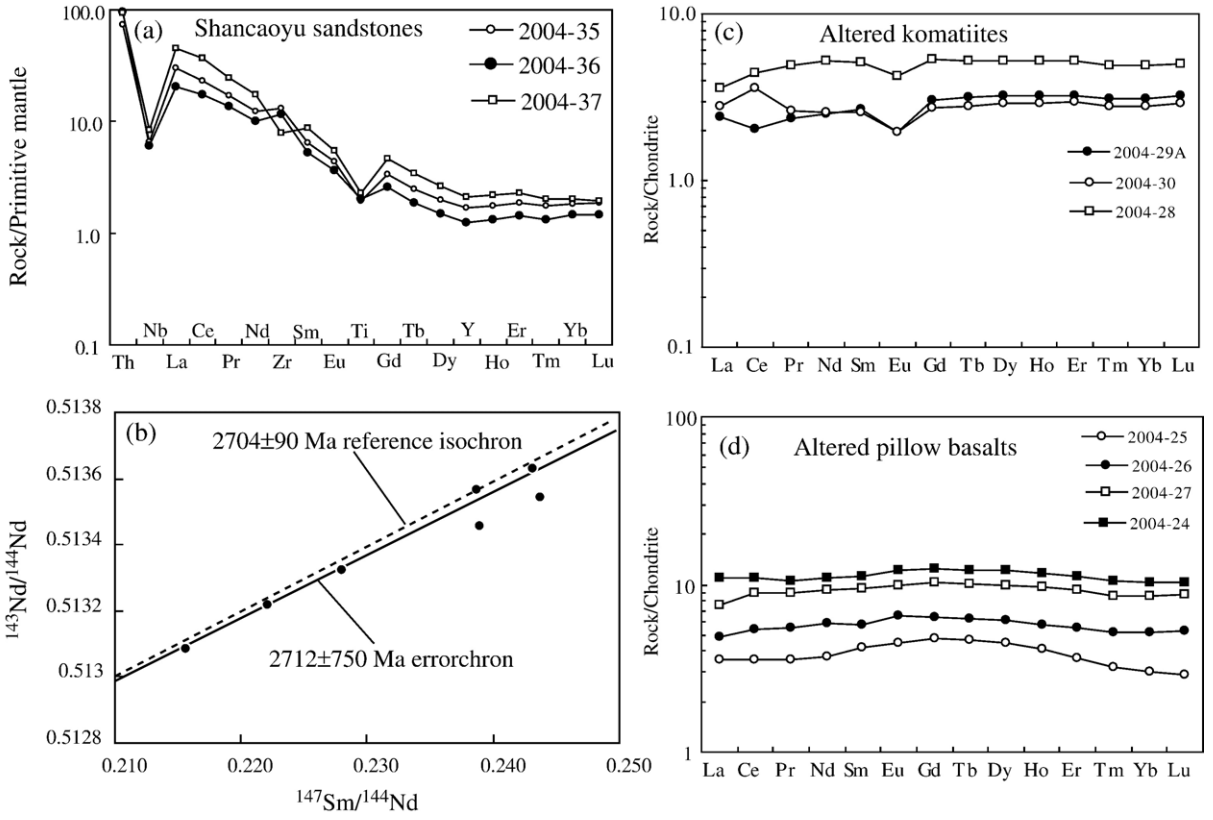


Fig. 9. (a) Primitive mantle-normalized trace element diagrams for sandstones. (b) $^{147}Sm/^{144}Nd$ versus $^{143}Nd/^{144}Nd$ variation diagram for the selected Taishan komatiites, yielding a 2712±750 Ma errorchron age (reference isochron age was obtained from regression of amphibolite data in Jahn et al., 1988). (c–d) Chondrite-normalized REE patterns for altered komatiites and pillow basalts in the upper Yanlingguan Formation. Normalization values are as in Fig. 8.

contamination process is unlikely, although the presence of unexposed sandstones, andesites, and rhyolites at the base of the volcanic sequence cannot be ruled out.

In the 2700 Ma Wawa subprovince, LREE-depleted AUK, LREE-enriched ADK, tholeiitic basalts with near-flat REE patterns, and LREE-enriched transitional to alkaline basalts are spatially and temporarily associated. Some tholeiitic basalts and AUK have variably negative Nb anomalies and small positive initial $\varepsilon_{Nd}$ values (+0.71 to +1.31), whereas ADK and transitional to alkaline basalts display HIMU-OIB-like positive Nb anomalies and large positive initial $\varepsilon_{Nd}$ values (+1.96 to +3.49), consistent with a heterogeneous depleted mantle plume (Polat et al., 1999). By comparison with the trace element–$\varepsilon_{Nd}$ systematics of Wawa uncontaminated komatiites and basalts the second process can be ruled out for the Taishan komatiites (cf. Polat et al., 1999).

Exposed 2800–2700 Ma TTG could have been the source of the contamination: however, TTG were emplaced into the greenstone belt (Cao et al., 1996), and are characterized by large positive initial $\varepsilon_{Nd}$ (~+3.3) values (Jahn et al., 1988), suggesting that they are not likely the source of contamination. Three possible processes may have removed the older basement rocks from beneath the Taishan belt between 2700–2600 Ma: (1) they might have been buried to the greater depths by crustal thickening; (2) they may have been reworked or assimilated by voluminous TTG magmatism; or (3) the greenstone cover was detached and displaced from the basement during collision.

In this study, a two-component (enriched and depleted) mixing model has been adopted to explain the origin of the concave-upward LREE patterns of the Taishan komatiites (Figs. 8 and 11a). The depleted component for this modeling was estimated by extrapolation of the HREE pattern of the isotopically

Table 5
Representative microprobe analyses of olivine compositions from the Taishan komatiites

| | Cumulate olivines | | | | | Spinifex | | | | | |
|---|---|---|---|---|---|---|---|---|---|---|---|
| | KM33 | | | KM37 | | KM3B | | | KM4 | | |
| | Olivine #1 ($n$=10) | Olivine #2 ($n$=10) | Olivine #3 ($n$=10) | Olivine #1 ($n$=10) | Olivine #2 ($n$=10) | Olivine #1 ($n$=9) | Olivine #2 ($n$=9) | Olivine #3 ($n$=10) | Olivine #1 ($n$=10) | Olivine #2 ($n$=10) | Olivine #3 ($n$=10) |
| $SiO_2$ | 39.87 | 39.66 | 39.71 | 39.78 | 39.93 | 39.14 | 38.95 | 38.82 | 38.94 | 39.02 | 39.14 |
| $TiO_2$ | 0.00 | 0.00 | 0.00 | 0.00 | 0.00 | 0.00 | 0.00 | 0.01 | 0.00 | 0.00 | 0.00 |
| $Al_2O_3$ | 0.00 | 0.00 | 0.00 | 0.00 | 0.00 | 0.00 | 0.00 | 0.00 | 0.00 | 0.00 | 0.00 |
| FeO | 14.67 | 14.68 | 14.93 | 14.87 | 15.03 | 18.85 | 18.73 | 19.14 | 18.53 | 18.35 | 18.37 |
| MnO | 0.24 | 0.28 | 0.29 | 0.30 | 0.30 | 0.41 | 0.39 | 0.39 | 0.31 | 0.33 | 0.29 |
| MgO | 44.36 | 43.93 | 44.38 | 44.42 | 44.08 | 41.23 | 41.48 | 41.28 | 41.90 | 42.08 | 41.87 |
| CaO | 0.00 | 0.00 | 0.01 | 0.01 | 0.01 | 0.01 | 0.01 | 0.01 | 0.05 | 0.01 | 0.01 |
| $K_2O$ | 0.00 | 0.00 | 0.00 | 0.00 | 0.00 | 0.00 | 0.00 | 0.00 | 0.00 | 0.00 | 0.00 |
| $Na_2O$ | 0.00 | 0.01 | 0.02 | 0.01 | 0.01 | 0.02 | 0.01 | 0.01 | 0.00 | 0.00 | 0.01 |
| $P_2O_5$ | 0.00 | 0.01 | 0.01 | 0.01 | 0.01 | 0.01 | 0.01 | 0.01 | 0.01 | 0.01 | 0.02 |
| Sum | 99.54 | 99.01 | 99.80 | 99.82 | 99.57 | 100.04 | 99.96 | 100.07 | 100.13 | 100.19 | 100.06 |
| Fo (%) | 84.3 | 84.2 | 84.1 | 84.2 | 83.9 | 79.6 | 79.8 | 79.4 | 80.1 | 80.3 | 80.2 |
| Ni (ppm) | 3183 | 3395 | 3436 | 2947 | 3458 | 2680 | 2892 | 2841 | 2970 | 3087 | 3025 |

| | Spinifex | | | | | | | |
|---|---|---|---|---|---|---|---|---|
| | KM25 | | | KM7B | | | KM38 | |
| | Olivine #1 ($n$=10) | Olivine #2 ($n$=10) | Olivine #3 ($n$=10) | Olivine #1 ($n$=10) | Olivine #2 ($n$=10) | Olivine #1 ($n$=10) | Olivine #2 ($n$=10) | Olivine #3 ($n$=10) |
| $SiO_2$ | 39.07 | 38.88 | 38.97 | 39.06 | 38.91 | 39.22 | 39.16 | 39.33 |
| $TiO_2$ | 0.00 | 0.01 | 0.00 | 0.03 | 0.01 | 0.00 | 0.00 | 0.03 |
| $Al_2O_3$ | 0.00 | 0.00 | 0.00 | 0.00 | 0.00 | 0.00 | 0.00 | 0.00 |
| FeO | 18.84 | 19.62 | 19.54 | 18.86 | 18.97 | 18.29 | 18.23 | 17.88 |
| MnO | 0.39 | 0.37 | 0.36 | 0.35 | 0.35 | 0.31 | 0.32 | 0.31 |
| MgO | 41.22 | 40.50 | 40.81 | 41.29 | 41.51 | 41.78 | 42.03 | 42.14 |
| CaO | 0.01 | 0.00 | 0.01 | 0.01 | 0.01 | 0.02 | 0.00 | 0.01 |
| $K_2O$ | 0.00 | 0.00 | 0.00 | 0.00 | 0.00 | 0.00 | 0.00 | 0.00 |
| $Na_2O$ | 0.01 | 0.03 | 0.01 | 0.01 | 0.00 | 0.01 | 0.02 | 0.01 |
| $P_2O_5$ | 0.02 | 0.04 | 0.01 | 0.07 | 0.02 | 0.05 | 0.02 | 0.02 |
| Sum | 99.94 | 99.83 | 100.10 | 100.05 | 100.20 | 99.97 | 100.17 | 100.11 |
| Fo (%) | 79.6 | 78.6 | 78.8 | 79.6 | 79.6 | 80.3 | 80.4 | 80.8 |
| Ni (ppm) | 2815 | 2954 | 2932 | 2873 | 3017 | 2953 | 2833 | 2880 |

and geochemically most depleted komatiite sample as representing the least contaminated parental magma (sample KM33, $\varepsilon_{Nd}$=+3.6), assuming monotonically decreasing chondrite-normalized MREE and LREE values. Given the absence of representative older basement rocks beneath the Taishan belt, the enriched component was calculated from the average bulk composition of greywacke sandstones (Figs. 3, 5a, and 9a; Table 4), assuming that they were derived from the exposed continental basement during the emplacement of komatiites.

Table 6
Sm–Nd concentrations and isotopic ratios for the selected Taishan komatiites

| | Nd (ppm) | Sm (ppm) | $^{147}Sm/^{144}Nd$ | $^{143}Nd/^{144}Nd$ | $\varepsilon_{Nd}$ (2704 Ma) |
|---|---|---|---|---|---|
| KM3B | 1.21 | 0.49 | 0.245 | 0.513505±50 | 0.04 |
| KM4 | 1.11 | 0.46 | 0.248 | 0.513535±14 | −0.38 |
| KM7B | 0.82 | 0.29 | 0.216 | 0.513085±11 | 2.15 |
| KM25 | 0.75 | 0.28 | 0.222 | 0.513217±10 | 2.46 |
| KM38 | 0.93 | 0.37 | 0.239 | 0.513457±14 | 1.29 |
| KM40 | 0.69 | 0.28 | 0.244 | 0.513544±17 | 1.32 |
| KM 33 | 0.40 | 0.16 | 0.239 | 0.513567±15 | 3.57 |
| KM 37 | 0.41 | 0.16 | 0.243 | 0.513628±13 | 3.20 |

Results of the mixing calculations demonstrate that the observed LREE patterns of the komatiites can be explained by the assimilation of up to 6% of the continental basement (Fig. 11a). The Taishan komatiites plot in the same field as crustally contaminated Archean komatiites on $Th/Nb_{pm}$ and $La/Nb_{pm}$ space (Fig. 11b). Similarly, there are strong correlations between initial $\varepsilon_{Nd}$ values and elements (e.g., Ni, MgO, $TiO_2$, Zr and LREE) sensitive to assimilation-

Table 7
Geochemical of compositions of olivine, chlorite, amphibole, and serpentine in sample KM3A

| Mineral modal abundance | Olivine ($n$=28) (0–10%) | Chlorite ($n$=5) (0–10%) | Amphibole ($n$=5) (10–20%) | Serpentine ($n$=5) (60–90%) | Whole rock |
|---|---|---|---|---|---|
| $SiO_2$ | 39.0 | 34.8 | 53.9 | 49.0 | 45.9 |
| $TiO_2$ | 0.002 | 0.09 | 0.37 | 0.07 | 0.21 |
| $Al_2O_3$ | 0.002 | 23.07 | 5.18 | 0.07 | 5.17 |
| FeO | 18.9 | 7.0 | 4.2 | 4.3 | 10.1 |
| MnO | 0.40 | 0.02 | 0.13 | 0.07 | 0.14 |
| MgO | 41.3 | 34.8 | 21.5 | 46.1 | 31.8 |
| CaO | 0.01 | 0.03 | 13.26 | 0.11 | 6.19 |
| $K_2O$ | n.d. | n.d | n.d | n.d | 0.03 |
| $Na_2O$ | 0.01 | 0.24 | 1.38 | 0.19 | 0.47 |
| $P_2O_5$ | 0.01 | n.d | n.d | n.d | 0.01 |
| $Cr_2O_3$ | n.d | 0.85 | 0.63 | 0.03 | |
| NiO | 0.33 | 0.25 | 0.08 | 0.33 | |
| Mg-number | 79.6 | 89.8 | 90.1 | 95.0 | 84.9 |

n.d.: not determined.

fractional crystallization (AFC), suggesting that the geochemical characteristics of the Taishan komatiites resulted from combined olivine fractionation and crustal contamination (Fig. 10).

### 6.4. Type of komatiite

Recently, a classification scheme has been developed for mafic and ultramafic volcanic rocks, including komatiites, based on a [$TiO_2$] versus [$Al_2O_3$] variation diagram, where [$Al_2O_3$] and [$TiO_2$] are contents of these components in mole proportions (normalized to unity) as projected from the olivine composition (see Hanski et al., 2001). Although komatiites in the Taishan belt are crustally contaminated, the effects of contamination are minor on $Al_2O_3/TiO_2$ ratios because both elements show similar degrees of correlation with initial $\varepsilon_{Nd}$ values (Fig. 10c, d). In [$Al_2O_3$]–[$TiO_2$] coordinate space, the Taishan komatiites plot mostly in the Al-depleted komatiite field (Fig. 11c, d). However, they lack the LREE-enriched characteristic patterns of the Al-depleted Barberton komatiites stemming from residual garnet in the source (Lahaye et al., 1995; Parman et al., 2003). On the [$TiO_2$] versus $Gd/Yb_{pm}$ diagram of Sproule et al. (2002), the Taishan komatiites plot in the Ti-depleted field (Fig. 11d).

## 7. Implications for geodynamic history

The presence of gneissic, granitic, and amphibolitic clasts in conglomerates, and zircon and apatite xenocrysts in komatiites indirectly imply the existence of older continental basement during deposition of the Taishan belt. Similarly, the petrographic and geochemical characteristics of associated sandstones are consistent with a proximal continental source area. The presence of pillow basalts and banded iron formations in the belt suggests that its deposition took place in a submarine basin. Coarse-grained sandstones and conglomerates are consistent with a shallow depositional environment. These geological features collectively suggest that the geodynamic evolution of the Taishan greenstone belt began on a stable/or passive continental margin between 2800 and 2700 Ma.

The Taishan komatiites are distinctive in that they have higher MgO and Ni, but lower $TiO_2$, Zr, HREE, and Y concentrations than other Archean or Phanerozoic counterparts (Fig. 12; Table 3). Such compositional features signify a more refractory mantle source, higher degree of partial melting, or some combination of the two (Fig. 12; Table 3; cf. Herzberg, 1992, 2004; and references therein). The trace element and Nd isotope systematics of komatiites are consistent with 2–6% crustal contamination. Primitive mantle-normalized trace element patterns of inter-layered pillow basalts are comparable to those of crustally contaminated komatiites and komatiitic basalts of other Archean greenstone belts (cf. Jochum et al., 1991). Accordingly, the high-temperature komatiitic melts likely have interacted with older crustal rocks during their ascent to the surface, or assimilated sedimentary or felsic volcanic rocks at the surface (cf. Barrie, 1999; Wyman, 1999; Wyman et al., 1999).

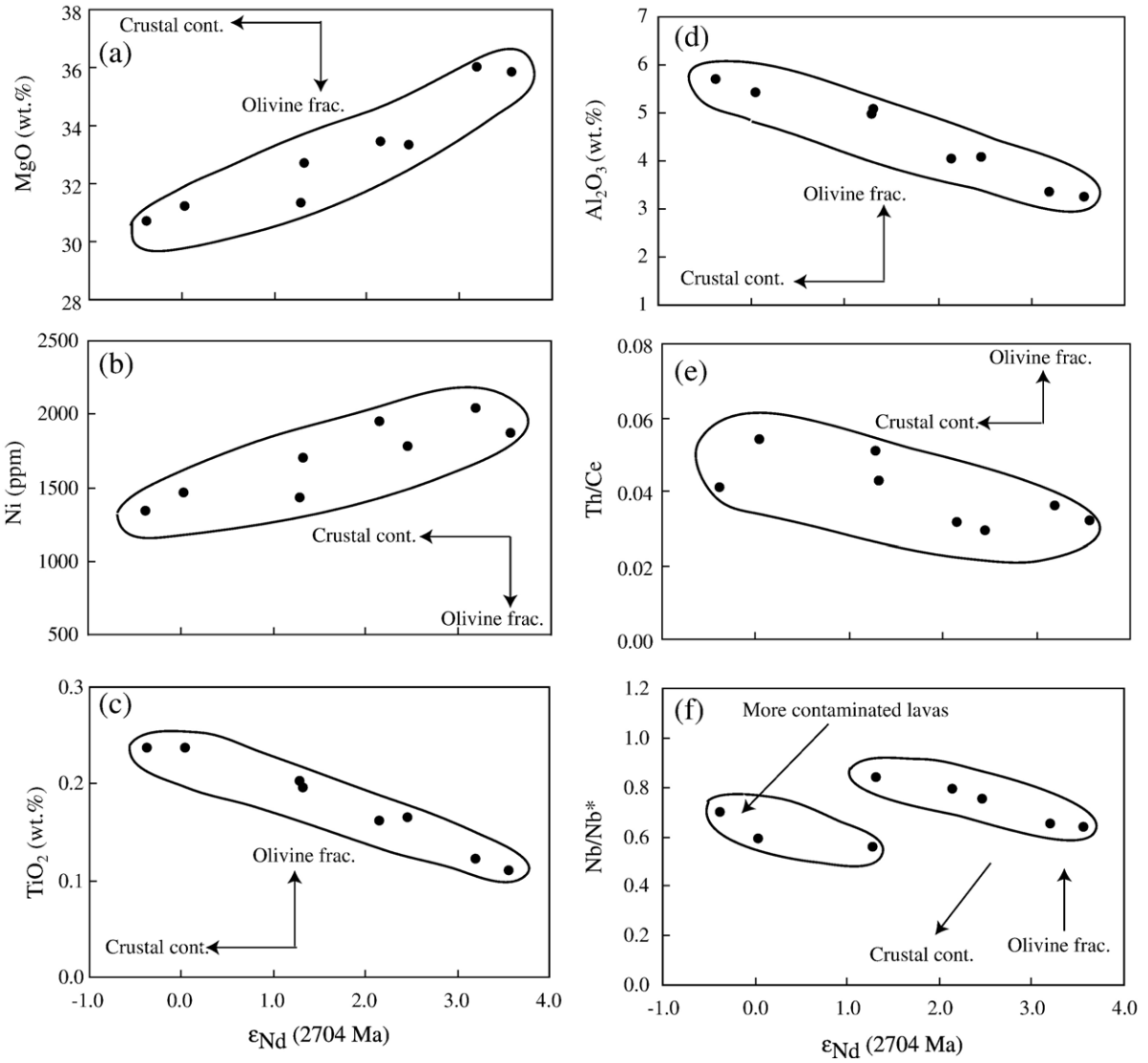


Fig. 10. Initial $\varepsilon_{Nd}$ versus selected major and trace element variation diagrams. More contaminated samples are displaced towards the lower Nb/Nb* values, indicating that the negative Nb anomalies were produced by crustal contamination.

If the Taishan komatiites were derived from a mantle plume, their geochemistry, like those of the Kambalda komatiites and associated basalts (Sylvester et al., 1997; Arndt et al., 2001), may record mantle plume–craton interaction at ~2700 Ma. Interaction between the early Cretaceous Kerguelen mantle plume and eastern Gondwanaland (see Mahoney et al., 1995; Frey et al., 2002) would be a good Phanerozoic analog for the interaction between the Taishan plume and the North China Craton.

The Taishan greenstone belt was intruded by TTG plutons and underwent amphibolite-grade regional metamorphism during a collision event at ~2700 Ma (Cao et al., 1996). The TTG are characterized by high-Al ($Al_2O_3$=16–19 wt.%) and Na ($Na_2O$=3.8–5.1 wt.%) concentrations, strongly fractionated REE patterns ($La/Yb_{cn}$=14–50; $Gd/Yb_{cn}$=3.3–6.2), and high $Al_2O_3/TiO_2$ (30–100) and Sr/Y (50–100) ratios (Cao et al., 1996). These geochemical characteristics are consistent with a subduction zone geochemical signature (Drummond et al., 1996; and references therein). The belt was further intruded by the 2700–2600 Ma subduction zone gabbros and diorites (Cao et al., 1996). Collectively,

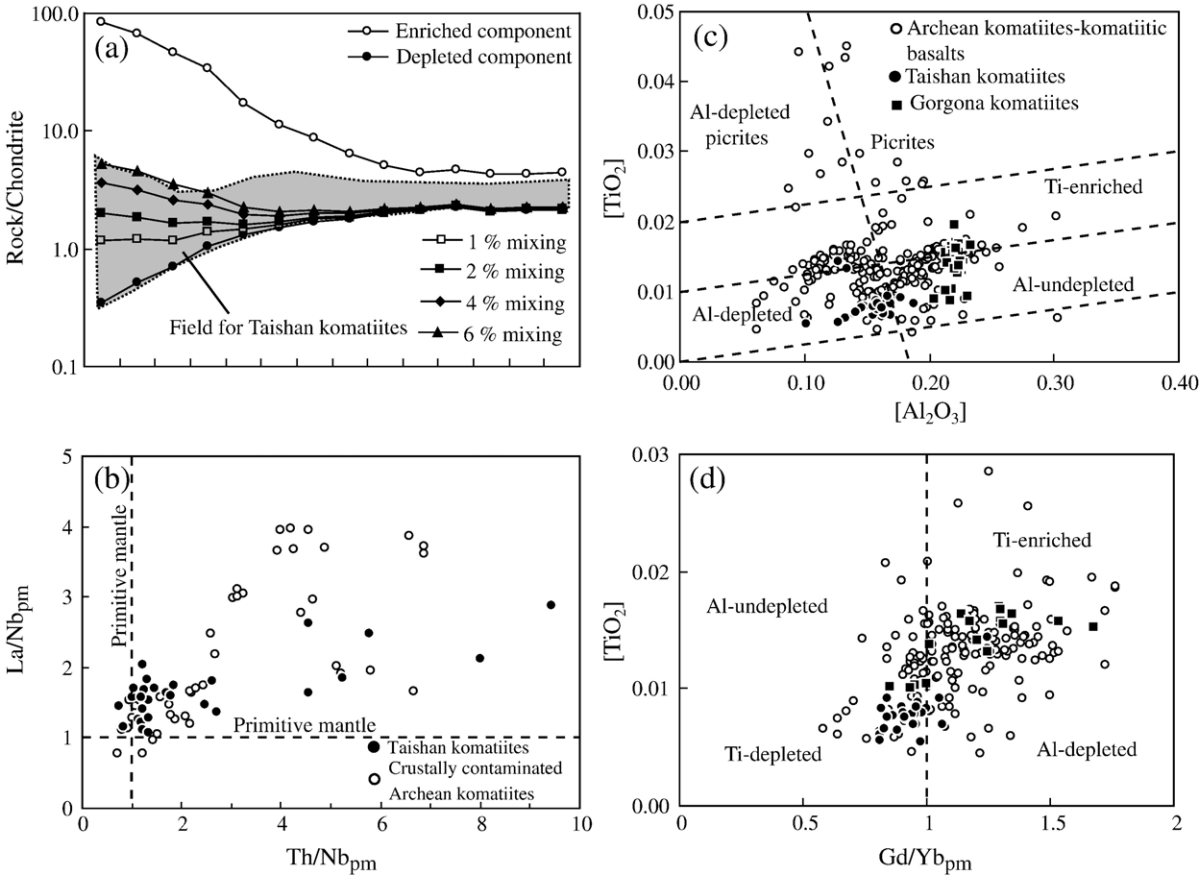


Fig. 11. (a) Two-component mixing model. The patterns produced by mixing calculations are comparable to those of the Taishan komatiites (shaded area), consistent with 2–6% crustal contamination of these lavas. (b) $Th/Nb_{pm}$ versus $La/Nb_{pm}$ diagram, suggesting crustal contamination for the Taishan komatiites. (c–d) $[Al_2O_3]$ versus $[TiO_2]$, and $Al_2O_3/TiO_2$ versus $Gd/Yb_{pm}$ variation diagrams, comparing the Taishan komatiites, Archean komatiites and komatiitic basalts, and Gorgona komatiites. Data for the crustally contaminated komatiites are from Hollings and Kerrich (1999), Hollings et al. (1999), Perring et al. (1996), Puchtel et al. (1997). Archean komatiite–komatiitic basalt data are from Dostal and Mueller (1997), Fan and Kerrich (1997), Jochum et al. (1991), Lahaye et al. (1995), Maurice et al. (2003), Nisbet et al. (1987), Polat et al. (1999), Puchtel et al. (1993, 1998, 1999), Rollinson (1999), Sproule et al. (2002), Tomlinson et al. (1999), Wilson et al. (1989), and Xie and Kerrich (1994). Gorgona data are from Kerr (published and unpublished data). $[Al_2O_3]$ and $[TiO_2]$ values were calculated using the formulas of Hanski et al. (2001), where $[Al_2O_3] = Al_2O_3/(2/3 - MgO - FeO)$, $[TiO_2] = TiO_2/(2/3 - MgO - FeO)$.

these geological processes suggest that the geodynamic setting of the Taishan belt changed from a passive to an active continental margin between 2700 and 2600 Ma.

Although the geochemical and field characteristics of the Taishan greenstone belt can be best explained by a plume–craton interaction, an alternative subduction zone geodynamic setting cannot be ruled out. The presence of calc-alkaline andesitic to rhyolitic volcanic rocks in the supracrustal sequence and subduction zone geochemical signatures in the spatially associated TTGs can also be explained by an arc–plume interaction model (see Dostal and Mueller, 1997; Wyman, 1999; Wyman et al., 1999). According to Parman and co-workers (1997, 2003), Archean komatiites are compositionally comparable to Phanerozoic boninites; therefore, they may have formed as arc lavas by hydrous melting of the metasomatized sub-arc mantle wedge. As a matter of fact, REE patterns and negative Nb anomalies of the cumulate Taishan komatiites are similar to those of Archean and Phanerozoic boninites (see Fig. 8a; Polat et al., 2002; and references therein). The Taishan komatiites, however, have higher Ti/Zr and Ti/V, but lower $Al_2O_3/TiO_2$ and Zr/Sm ratios than boninites. Additionally, they possess higher MgO and

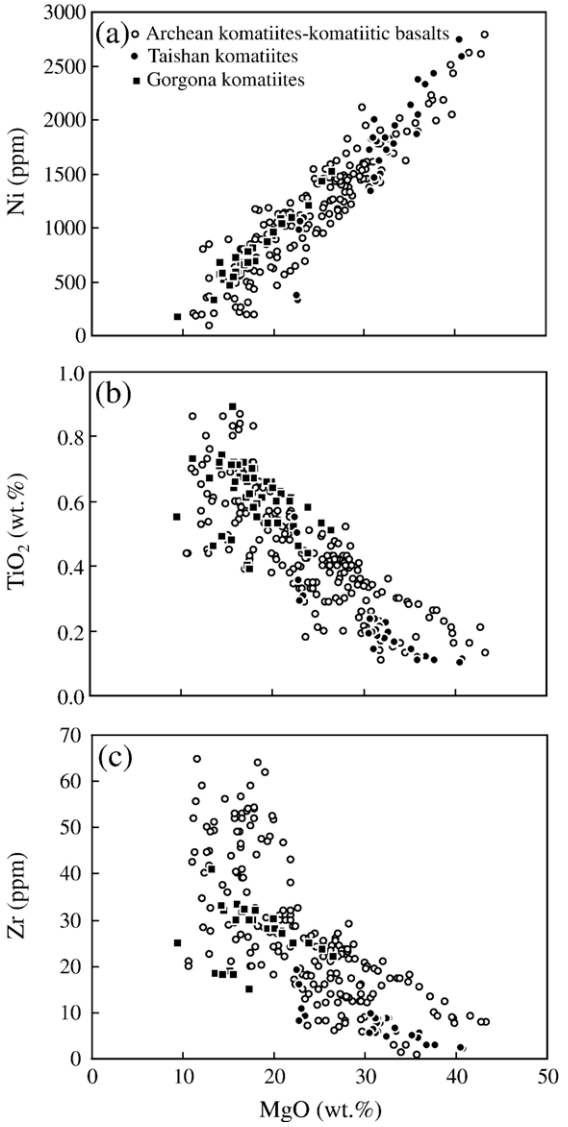


Fig. 12. MgO versus Ni, $TiO_2$, and Zr variation diagrams, comparing the Taishan komatiites, other Archean komatiites and komatiitic basalts, and Gorgona komatiites. Data sources are as in Fig. 11.

Ni, but lower $Al_2O_3$ and $SiO_2$ contents compared to boninites, collectively inconsistent with a boninitic composition.

## Acknowledgements

We thank C. Herzberg, R. Kerrich, S. Parman, and A. Trenhaile for reviewing the initial draft of the manuscript. A.C. Kerr is acknowledged for providing unpublished data from Gorgona komatiites. T. Bonli, J. C. Barrette, Z. Yang, and B. Cousens are acknowledged for their help during geochemical analyses. Constructive reviews by D. Wyman and an anonymous reviewer have resulted in significant improvements to the paper. This is a contribution of NSERC grants 250926 to AP and 83117 to BF. Field work was supported by National Science Foundation (USA) grant awarded to T. Kusky, and NNSF grant awarded to J. H. Li. **[SG]**

## References

Arndt, N.T., 1994. Archean komatiites. In: Condie, K.C. (Ed.), Archean Crustal Evolution. Elsevier, Amsterdam, pp. 11–44.

Arndt, N.T., Ginibre, C., Chauvel, C., Albarède, F., Cheadle, M., Jenner, G., Lahaye, Y., 1998. Were komatiites wet? Geology 26, 739–742.

Arndt, N.T., Bruzak, G., Reischmann, T., 2001. The oldest continental and oceanic plateaus—geochemistry of basalts and komatiites of the Pilbara Craton, Australia. In: Buchan, K.L., Ernst, R.E. (Eds.), Mantle Plumes: Their Identification Through Time. Geol. Soc. Am. Spec. Paper, vol. 352, pp. 1–30.

Barrie, C.T., 1999. Komatiite flows of Kidd Creek footwall, Abitibi Subprovince, Canada. Econ. Geol. Monogr. 10, 143–161.

Cao, G., Wang, Z., Cheng, Z., Dong, Y., Li, P., Wang, S., Jin, L., Shen, K., Xu, J., Shen, K., Shi, Y., Xu, H., Zhan, C., Zheng, L., Zhang, Z., Ren, X., Zai, Y., Ma, Y., Liang, B., 1996. Early Precambrian Geology of Western Shandong. Geological Publishing House, Beijing, pp. 1–210 (in Chinese with English Abstract).

Dostal, J., Mueller, W.U., 1997. Komatiite flooding of a rifted Archean rhyolitic arc complex: geochemical signature and tectonic significance of the Stoughton–Roquemaure Group, Abitibi greenstone belt, Canada. J. Geol. 105, 545–563.

Dostal, J., Mueller, W.U., 2004. Komatiite geochemistry. In: Eriksson, P.G., Altermann, W., Nelson, D., Mueller, R., Catuneanu, W.U. (Eds.), The Precambrian Earth: Tempos and Events. Elsevier, Amsterdam, pp. 290–298.

Drummond, M.S., Defant, M.J., Kepezhinskas, P.K., 1996. Petrogenesis of slab-derived trondhjemite–tonalite–dacite/adakite magmas. Trans. R. Soc. Edinb. Earth Sci. 87, 205–215.

Fan, J., Kerrich, R., 1997. Geochemical characteristics of aluminium depleted and undepleted komatiites and HFSE-enriched low-Ti tholeiites, western Abitibi greenstone belt: a heterogeneous mantle plume-convergent margin environment. Geochim. Cosmochim. Acta 61, 4723–4744.

Frey, F.A., Weis, D., Borisova, A.Y., Xu, G., 2002. Involvement of continental crust in the formation of the Cretaceous Kerguelen Plateau: new perspectives from ODP Leg 120 sites. J. Petrol. 43, 1207–1239.

Gibson, S.A., 2002. Major element heterogeneity in Archean to Recent mantle plume starting-heads. Earth Planet. Sci. Lett. 195, 59–74.

Grove, T.L., Parman, S.W., 2004. Thermal evolution of the Earth as recorded by komatiites. Earth Planet. Sci. Lett. 219, 173–187.

Hanski, E., Huhma, H., Rastas, P., Kamenetsky, V.S., 2001. The Palaeoproterozoic komatiite–picrite association of Finnish Lapland. J. Petrol. 42, 855–876.

Herzberg, C., 1992. Depth and degree of melting of komatiites. J. Geophys. Res. 97, 4521–4540.

Herzberg, C., 2004. Geodynamic information in peridotite petrology. J. Petrol. 45, 2507–2530.

Hofmann, A.W., 1988. Chemical differentiation of the Earth: the relationships between mantle, continental crust, and oceanic crust. Earth Planet. Sci. Lett. 90, 297–314.

Hollings, P., Kerrich, R., 1999. Trace element systematics of ultramafic and mafic volcanic rocks from the 3 Ga North Caribou greenstone belt, Northwestern Superior Province. Precambrian Res. 93, 257–279.

Hollings, P., Wyman, D., Kerrich, R., 1999. Komatiite–basalt–rhyolite volcanic association in Northern Superior Province greenstone belts: significance of plume–arc interaction in the generation of the proto continental Superior Province. Lithos 46, 137–161.

Jahn, B.M., Auray, B., Shen, Q.H., Liu, D.Y., Zhang, Z.Q., Dong, Y.J., Ye, X.J., Zhang, Q.Z., Cornichet, J., Mace, J., 1988. Archean crustal evolution in China: the Taishan Complex, and evidence for juvenile crustal addition from long-term depleted mantle. Precambrian Res. 38, 381–403.

Jacobsen, S.B., Wasserburg, G.J., 1980. Sm–Nd isotopic evolution of chondrites. Earth Planet. Sci. Lett. 50, 139–155.

Jenner, G.A., Longerich, H.P., Jackson, S.E., Fryer, B.J., 1990. ICP-MS — a powerful tool for high precision trace element analysis in earth sciences: evidence from analysis of selected U.S.G.S. Reference samples. Chem. Geol. 83, 133–148.

Jochum, K.P., Arndt, N.T., Hofmann, A.W., 1991. Nb–Th–La in komatiites and basalts: constraints on komatiite petrogenesis and mantle evolution. Earth Planet. Sci. Lett. 107, 272–289.

Kerr, A.C., Marriner, G.F., Arndt, N.T., Tarney, J., Nivia, A., Saunders, A.D., Duncann, R.A., 1996. The petrogenesis of Gorgona komatiites, picrites, and basalts: new field, petrographic and geochemical constraints. Lithos 37, 245–260.

Kusky, T.M., Li, J.H., 2003. Paleoproterozoic tectonic evolution of the North China Craton. J. Asian Earth Sci. 22, 383–397.

Lahaye, Y., Arndt, N., Byerly, G., Chauvel, C., Fourcad, S., Gruau, G., 1995. The influence of alteration on the trace element and Nd isotopic compositions of komatiites. Chem. Geol. 126, 43–64.

Ludwig, K., 2001. User's manual for Isoplot/Ex Version 2.49. A Geochronological toolkit for Microsoft Excel. Special Publication, vol. 1a. Berkeley Geochronology Center.

Ma, Y., 1996. Geological characteristics of the Archean greenstone belt in Western Shandong. Proceeding of Shandong Geology and Mineral Deposits. Shandong Science and Technology Press, Jinan, pp. 22–32 (in Chinese with English Abstract).

Mahoney, J.J., Jones, W.B., Frey, F.A., Salters, V.J.M., Pyle, D.G., Davies, H.L., 1995. Geochemical characteristics of lavas from Broken Ridge, the Naturaliste Plateau and southernmost Kerguelen Plateau: Cretaceous plateau volcanism in the southeast Indian Ocean. Chem. Geol. 120, 315–345.

Maurice, C., Francis, D., Madore, L., 2003. Constraints on early Archean crustal extraction and tholeiitic–komatiitic volcanism in greenstone belts of the Northern Superior Province. Can. J. Earth Sci. 40, 431–445.

McDonough, W.F., Ireland, T.R., 1993. Intraplate origin of komatiites inferred from trace elements in glass inclusions. Nature 365, 432–434.

Nesbitt, R.W., Sun, S.-S., Purvis, A.C., 1979. Komatiites: geochemistry and genesis. Can. Mineral. 17, 165–186.

Nisbet, E.G., 1982. The tectonic setting and petrogenesis of komatiites. In: Arndt, N.T., Nisbet, E.G. (Eds.), Komatiites. George Allen and Unwin, London, pp. 501–520.

Nisbet, E.G., Arndt, N.T., Bickle, M.J., Cameron, W.E., Chauvel, C., Cheadle, C., Hegner, E., Kyser, K., Martin, A., Renner, R., Roedder, E., 1987. Uniquely fresh 2.7 Ga komatiites from the Belingwe greenstone belt, Zimbabwe. Geology 15, 1147–1150.

Nisbet, E.G., Cheadle, M.J., Arndt, N.T., Bickle, M.J., 1993. Constraining the potential temperature of the Archean mantle: review of the evidence from komatiites. Lithos 30, 291–307.

Parman, S.W., Dann, J.C., Grove, T.L., de Wit, M.J., 1997. Emplacement conditions of komatiite magmas from the 3.49 Ga Komati Formation, Barberton Greenstone belt, South Africa. Earth Planet. Sci. Lett. 150, 303–323.

Parman, S.W., Grove, T.L., Dann, J.C., 2001. The production of Barberton komatiites in an Archean subduction zone. Geophys. Res. Lett. 28, 2513–2516.

Parman, S., Shimizu, N., Grove, T.L., Dann, J.C., 2003. Constraints on the pre-metamorphic trace element composition of Barberton komatiites from ion probe analyses of preserved clinopyroxene. Contrib. Mineral. Petrol. 144, 383–396.

Perring, C.S., Barnes, S.J., Hill, R.E.T., 1996. Geochemistry of komatiites from Forrestania, Southern Cross Province, Western Australia: evidence for crustal contamination. Lithos 37, 181–197.

Polat, A., Hofmann, A.W., 2003. Alteration and geochemical patterns in the 3.7–3.8 Ga Isua greenstone belt, West Greenland. Precambrian Res. 126, 197–218.

Polat, A., Kerrich, R., Wyman, D.A., 1999. Geochemical diversity in oceanic komatiites and basalts from the late Archean Wawa greenstone belts, Superior Province, Canada: trace element and Nd isotope evidence for a heterogeneous mantle. Precambrian Res. 94, 139–173.

Polat, A., Hofmann, A.W., Rosing, M.T., 2002. Boninite-like volcanic rocks in the 3.7–3.8 Ga Isua greenstone belt, West Greenland: geochemical evidence for intra-oceanic subduction zone processes in the early Earth. Chem. Geol. 184, 231–254.

Puchtel, I.S., Zhuravlev, D.Z., Samsonov, A.V., Arndt, N.T., 1993. Petrology and geochemistry of metamorphosed komatiites and basalts from the Tungurcha greenstone belt, Aldan Shield. Precambrian Res. 62, 399–417.

Puchtel, I.S., Haase, K.M., Hofmann, A.W., Chauvel, C., Kulikov, V. S., 1997. Petrology and geochemistry of crustally contaminated komatiitic basalts from the Vetreny belt, southeastern Baltic Shield: evidence for an early Proterozoic mantle plume beneath the rifted Archean continental lithosphere. Geochim. Cosmochim. Acta 61, 1205–1222.

Puchtel, I.S., Hofmann, A.W., Mezger, K., Jochum, K.P., Shchipansky, A.A., Samsonov, A.V., 1998. Oceanic plateau model for continental crustal growth in the Archean: a case study from the Kostomuksha greenstone belt, NW Baltic Shield. Earth Planet. Sci. Lett. 155, 57–74.

Puchtel, I.S., Hofmann, A.W., Amelin, Y.V., Garbe-Schönberg, C.D., Samsonov, A.V., Shchipansky, A.A., 1999. Combined mantle plume–island arc model for the formation of the 2.9 Ga Sumezero–Kenozero greenstone belt, SE Baltic Shield: isotope and trace element constraints. Geochim. Cosmochim. Acta 63, 3579–3595.

Renner, R., Nisbet, E.G., Cheadle, M.J., Arndt, N.T., Bickle, M.J., Cameron, W.E., 1994. Belingwe Belt, Zimbabwe: I. Petrography and mineralogy. J. Petrol. 35, 361–400.

Richard, P., Shimizu, N., Allègre, C.J., 1976. $^{143}Nd/^{146}Nd$, a natural tracer: an application to oceanic basalts. Earth Planet. Sci. Lett. 31, 269–278.

Rollinson, H., 1999. Petrology and geochemistry of metamorphosed komatiites and basalts from the Sula Mountains greenstone belt, Sierra Leone. Contrib. Mineral. Petrol. 134, 86–101.

Rudnick, R., Gao, S., 2004. Composition of the continental crust. In: Rudnick, R.L. (Ed.); Holland, H.D. Turekian, K.K. (Executive editors), Treatise on Geochemistry, volume 3, Elsevier, Amsterdam, pp. 1–64.

Sproule, R.A., Lesher, C.M., Ayer, J.A., Thurston, P.C., Herzberg, C., 2002. Spatial and temporal variations in the geochemistry of komatiites and komatiitic basalts in the Abitibi greenstone belt. Precambrian Res. 115, 153–186.

Sun, S.S., 1987. Chemical composition of Archean komatiites: implications for early history of the Earth and mantle evolution. J. Volcanol. Geother. Res. 32, 67–82.

Sun, S.S., McDonough, W.F., 1989. Chemical and isotopic systematics of oceanic basalts: implications for mantle composition and processes. In: Saunders, A.D., Norry, M.J. (Eds.), Magmatism in the Ocean Basins. Geol. Soc. Lond. Spec. Publ., vol. 42, pp. 313–345.

Sun, S.S., Nesbitt, R.W., McCulloch, M.T., 1989. Geochemistry and petrogenesis of Archean and early Proterozoic siliceous high-magnesian basalts. In: Crawford, A.J. (Ed.), Boninites and Related Rocks. Unwin Hyman, pp. 149–173.

Sylvester, P.J., Campbell, I.H., Bowyer, D.A., 1997. Niobium/Uranium evidence for early formation of the continental crust. Science 275, 521–523.

Taylor, S.R., McLennan, S.M., 1985. The Continental Crust: Its Composition and Evolution. Blackwell, Oxford. 312 pp.

Taylor, S.R., McLennan, S.M., 1995. The geochemical evolution of the continental crust. Rev. Geophys. 33, 241–265.

Tomlinson, K.T., Hughes, D.J., Thurston, P.C., Hall, R.P., 1999. Plume magmatism and crustal growth at 2.9 to 3.0 Ga in the Steep Rock and Lumby Lake area, Western Superior Province. Lithos 46, 103–136.

Wilson, A.H., 2003. A new class of silica enriched, highly depleted komatiites in the southern Kaapvaal Craton, South Africa. Precambrian Res. 127, 125–141.

Wilson, A.H., Versfeld, J.A., Hunter, D.R., 1989. Emplacement, crystallization, and alteration of spinifex-textured komatiitic basalt flows in the Archean Nondweni greenstone belt, southern Kaapvaal Craton, South Africa. Contrib. Mineral. Petrol. 101, 301–317.

Wilson, A.H., Shirey, S.B., Carlson, R.W., 2003. Archean ultra-depleted komatiites formed by hydrous melting of cratonic mantle. Nature 423, 858–861.

Wu, J.S., Geng, Y.S., Shen, Q.H., Liu, D.Y., Li, Z.L., Zhao, D.M., 1991. The Early Precambrian Significant Geological Events in the North China Craton. Geological Publishing House, Beijing, p. 115 (in Chinese).

Wu, J.S., Geng, Y.S., Shen, Q.H., Wan, Y.S., Liu, D.Y., Song, B., 1998. Archean Geology Characteristics and Tectonic Evolution of China-Korean Paleo-Continent. Geological Publishing House, Beijing, p. 212 (in Chinese).

Wyman, D.A., 1999. A 2.7 Ga depleted tholeiite suite: evidence of plume–arc interaction in the Abitibi greenstone belt, Canada. Precambrian Res. 97, 27–42.

Wyman, D.A., Bleeker, W., Kerrich, R., 1999. A 2.7 Ga plume, proto-arc, to arc transition and the geodynamic setting of the Kidd Creek deposit: evidence from precise ICP MS trace element data. Econ. Geol. Monogr. 10, 511–528.

Xie, Q., Kerrich, R., 1994. Silicate–perovskite and majorite signature komatiites from the Archean Abitibi greenstone belt: implications for early mantle differentiation and stratification. J. Geophys. Res. 99, 15799–15812.

Xie, Q., Kerrich, R., Fan, J., 1993. HFSE/REE fractionations recorded in three komatiite–basalt sequences, Archean Abitibi greenstone belt: implications for multiple plume sources and depths. Geochim. Cosmochim. Acta 57, 4111–4118.

Xu, H.F., Dong, Y.J., Shi, R.H., Jin, R.M., Shen, K., Li, X.G., 1992. The Granitoid–Greenstone Belts of Western Shangdong. Geological Publishing House, Beijing, pp. 1–83 (in Chinese with English abstract).

Zhang, R.S., Tang, H.S., Kong, L.G., Gan, Y.J., Song, B.Z., 2001. Characteristics and significance of the Sujiagou komatiite at Menying, Shandong. Reg. Geol. Chn. 20, 26–33 (in Chinese with English abstract).